

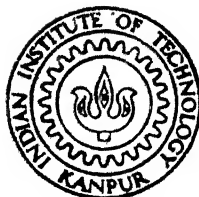
NUCLEATION AND GROWTH PHENOMENA DURING THE REDUCTION OF OXIDES OF SOME FCC METALS

by

SUKANTA CHATTERJEE

ME
1988
M

TH
ME/1988/M
e392n



DEPARTMENT OF METALLURGICAL ENGINEERING
INDIAN INSTITUTE OF TECHNOLOGY, KANPUR

APRIL, 1988

CHA
NUC

NUCLEATION AND GROWTH PHENOMENA DURING THE REDUCTION OF OXIDES OF SOME FCC METALS

A Thesis Submitted
In Partial Fulfilment of the Requirements
for the Degree of

MASTER OF TECHNOLOGY

{ . }

by

SUKANTA CHATTERJEE

to the

DEPARTMENT OF METALLURGICAL ENGINEERING
INDIAN INSTITUTE OF TECHNOLOGY, KANPUR

APRIL, 1988

13 APR 1989
CENTRAL LIBRARY
11 T APR

Acc. No. **A104133**

ME-1988-M-CHA-NUC

CERTIFICATE

20/4/88
V. K. Gupta

Certified that this work on "Nucleation and Growth Phenomena during the Reduction of Oxides of Some FCC Metals" has been carried out by Sukanta Chatterjee under our supervision and that it has not been submitted elsewhere for a degree.

Brahma Deo
(Dr. Brahma Deo)
Assistant Professor

R. K. Dube
(Dr. R.K. Dube)
Assistant Professor

Department of Metallurgical Engineering
Indian Institute of Technology Kanpur

April, 1988.

ACKNOWLEDGEMENTS

I take the opportunity to convey my deepest gratitude to my thesis supervisors, Dr. R.K. Dube and Dr. Brahma Deo for introducing me to this field, able guidance, lively interest throughout the work and fruitful suggestions.

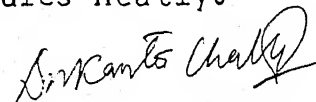
I wish to thank Dr. K.N. Rai, Professor, Department of Metallurgical Engineering, for his suggestions during the course of the study.

I am grateful to Dr. P.T. Rajagopalan, Scientist 'E', DMSRDE, Kanpur and Mr. Lal, NELMIF, BHU, Varanasi for their help for the scanning electron microscopy work during the present study.

I acknowledge the cooperation rendered by Mr. S.C. Soni, Metal Working Lab. and Mr. K.P. Mukherjee, Physical Metallurgy Lab. during my experimental work.

I am thankful to my colleague Mr. P.K. Bagdi and all those friends whose kind advice and cooperation inspired me during the course of my study.

Lastly I would thank Mr. U.S. Misra for typing the thesis and Mr. V.P. Gupta for drawing the figures neatly.


-SUKANTA CHATTERJEE

CONTENTS

	<u>Page</u>
LIST OF FIGURES	vi)
NOTATIONS	xi)
ABSTRACT	xiii)
 CHAPTER 1	
INTRODUCTION	1
1.1 Introduction	1
1.2 Phase Diagrams	4
1.3 Thermodynamic Stability of Iron Oxides	7
1.4 Crystal Structure of FCC Metals and their Oxides	7
1.4.1 Iron and its Oxides	7
1.4.2 Nickel and its Oxide	10
1.4.3 Copper and its Oxides	11
1.5 Formation of Nuclei and their Growth	11
1.6 Conditions leading to the Growth of Metals as a Layer or as a Whisker	14
1.6.1 Pure Metal Transport Control	15
1.6.2 Pure Oxygen Removal Control	17
1.6.3 Mixed Control	19
1.7 Mechanism and Morphology of Reduction Processes: A Review of Literature	19
1.7.1 Iron Oxide Reduction	19
1.7.2 Nickel Oxide Reduction	23
1.7.3 Copper Oxide Reduction	25
1.8 Scope of the Present Work	26
 CHAPTER 2	
EXPERIMENT	28
2.1 Description of the Reduction Apparatus	28
2.2 Raw Materials	29
2.3 Preparation of Compacts	29
2.4 Sintering and Reduction of Compacts	30
2.5 Specimen Preparation for Observation under Scanning Electron Microscope and Optical Microscope	32
 CHAPTER 3	
RESULTS AND DISCUSSION	34
3.1 Solid State Reduction of Hematite and Magnetite	34
3.1.1 The Model	34
3.1.2 Application of the Model to the Experimental Data	37
3.2 Mathematical Model for Gaseous Reduction of Iron Oxide	41
3.2.1 Introduction	41
3.2.2 Summary of Defects and Deviation from Stoichiometry	41

3.2.3	Phases and Phase Boundaries to be considered during Reduction	42
3.2.4	Balance of Defects	45
3.2.5	Calculation of Growth Rates	46
3.2.6	Application of Model to Experimental Data	50
3.2.7	Discussion	51
3.3	Formation and Growth of Fe, Ni, Cu Nuclei during Gaseous Reduction of their Oxides	53
3.3.1	Introduction	53
3.3.2	Results and Discussion	55
	(a) Shape of the Nuclei	56
	(b) Growth Rate of The Nuclei	62
	(c) Reduction of Dicalcium Ferrite Compacts	65
3.4	Morphology of the Reduction Process	68
3.4.1	Reduction of Iron Oxide Compacts	68
3.4.2	Reduction of Nickel Oxide Compacts	77
CHAPTER 4	CONCLUSIONS	81
CHAPTER 5	RECOMMENDATIONS FOR FUTURE WORK	84
REFERENCES		85

LIST OF FIGURES

<u>FIG. NO.</u>	<u>TITLE</u>	<u>PAGE</u>
1.1	Iron-oxygen system	5
1.2	Nickel-oxygen system	5
1.3	Copper-oxygen system	6
1.4	Thermodynamic region of stability between iron, wustite, magnetite and hematite	8
1.5	Metal activity curves and phase configuration in an oxide particle when reduced under pure metal transport control	16
1.6	Metal activity curves and phase configuration in an oxide particle when reduced under oxygen removal control	18
1.7	Metal activity curves and phase configuration in an oxide particle when reduced under mixed control	18
2.1	Specimen preparation	33
3.1	SEM of mixed hematite and iron compact to produce magnetite by solid state reduction	40
3.2	SEM of the same compact as in Fig. 3.1 after heating in nitrogen at 823K for 16 hours	40
3.3	Shape of the growing metal nuclei under pure metal transport control, pure oxygen removal control and combined metal transport and oxygen diffusion control	57

<u>FIG.NO.</u>	<u>TITLE</u>	<u>PAGE</u>
3.4	Schematic diagram showing the tetrahedral base pyramid in FCC unit cells	59
3.5	SEM of interfacial region of the partially reduced hematite (Reduction temperature - 1423K, Reductant - H_2) showing very first stage of nucleation	60
3.6	SEM of subsequent growth of the iron nuclei in Fig. 3.5 in the vertical direction leading to a bulge	60
3.7	SEM of the iron nuclei grown into a tetrahedral based pyramid	60
3.8	SEM of interfacial region of partially reduced nickel oxide (Reduction temperature- 1423K, Reductant - H_2) showing tetrahedral based pyramid shaped nickel nuclei	61
3.9	SEM of interfacial region of partially reduced cuprous oxide (Reduction temperature -873K, Reductant - H_2) showing tetrahedral based pyramid shaped copper nuclei	61
3.10	Mechanism of reduction of MeO to Me	63
3.11	SEM of interfacial region of partially reduced dicalcium ferrite (Reduction temperature -1373K , Reductant - H_2) showing tetrahedral based pyramid shaped iron nuclei	67

<u>FIG.NO.</u>	<u>TITLE</u>	<u>PAGE</u>
3.12	SEM of hematite concentrate powder showing no porosity	69
3.13	Optical micrograph of unreduced zone of partially reduced hematite (Reduction temperature -1423K , Reductant $-\text{H}_2$) showing fragmentation of oxide particles	69
3.14	SEM of partially reduced hematite (Reduction temperature -1423K , Reductant $-\text{H}_2$) showing fragmentation of particles in the interfacial region	69
3.15	Optical micrograph of partially reduced magnetite at the unreduced zone (Reduction temperature 1273K , Reductant $-\text{H}_2$) showing less cracking tendency of the oxide particles	69
3.16	Optical micrograph of partially reduced magnetite (Reduction temperature -1423K , Reductant $-\text{H}_2$) showing interface between reduced zone and unreduced zone	71
3.17	Optical micrograph of partially reduced magnetite (Reduction temperature -1423K , Reductant $-\text{H}_2$) showing some discontinuities during very early stage of iron formation on wustite	71

<u>FIG.NO.</u>	<u>TITLE</u>	<u>PAGE</u>
3.18	Optical micrograph of partially reduced magnetite compacts (Reduction temperature -1273K, Reductant $-H_2$) showing topochemical reduction of oxide particles	71
3.19	Optical micrograph of the interface in partially reduced hematite (Reduction temperature -1423K, Reductant $-H_2$) showing reduced zone and unreduced zone	75
3.20	Optical micrograph of partially reduced hematite (Reduction temperature -1098K, Reductant $-H_2$) showing topochemical reaction on individual particles	75
3.21	Optical micrograph of the interface of partially reduced nickel oxide (Reduction temperature -1423K, Reductant $-H_2$) showing reduced zone and unreduced zone.	78
3.22	Optical micrograph of partially reduced nickel oxide (Reduction temperature -823K, Reductant $-H_2$) showing topochemical reduction of oxide particles.	78
3.23	Optical micrograph of partially reduced nickel oxide in the interfacial zone (Reduction temperature -1423K, Reductant $-H_2$) showing long wavy stringers	80

<u>FIG.NO.</u>	<u>TITLE</u>	<u>PAGE</u>
3.24	Optical micrograph of partially reduced nickel oxide in the fully reduced zone (Reduction temperature -1423K, Reductant -H ₂) showing wavy stringer structure of nickel	80
3.25	Optical micrograph of partially reduced nickel oxide (Reduction temperature -1423K, Reductant -H ₂) showing very dense nickel structure.	80

NOTATIONS

A	total area of contact between the oxide and metal.
a_{Me}^I	activity of Me in MeO at the MeO/H ₂ interface.
a_{Me}^{II}	activity of Me in MeO adjacent to Me particles.
C_{Me}	average Me concentration of Me in MeO.
D	diffusion coefficient.
e'	free electron.
f	a factor in relation with growth ratio between Fe ₃ O ₄ and FeO.
f_{Me}	correlation factor for Me in MeO.
Fe _i	positively charged interstitial iron ions
h [•]	positively charged hole.
I _A	rate of growth of layer A (Fe ₂ O ₃).
I _B	rate of growth of layer B (Fe ₃ O ₄).
I _C	rate of growth of layer C (FeO).
I _D	rate of growth of layer D (Fe).
I _{Fe}	rate of Fe-transfer
i _n	rate of nth reaction.
I _O	rate of oxygen-transfer
J _{Me}	flux of Me through MeO.
K	number of particles per unit area of surface.
K ₁ & K ₂	constants depending on diffusion and oxygen potential gradient.
Me _{Me}	Me atom in MeO in its normal lattice site.
n	charge of vacancy.
P	ratio I _A /I _B .

$p(\text{O}_2)$	partial pressure of oxygen.
r	average radius of individual contact area.
R	ratio I_B/I_C .
s_{MeO}	thickness of MeO layer.
t	time
V_1	volume of 4-moles of FeO.
V_2	volume of 3-moles of Fe_3O_4 .
$V_{\text{Me}}^{n'}$	charged metal vacancy.
V_i	unoccupied interstitial site.
$V_{\text{O}}^{\bullet\bullet}$	positively charged oxygen vacancies.
X_1	thickness of FeO layer.
X_2	thickness of Fe_3O_4 layer.
u, x, y, z	proportion of vacant iron in lattice positions relative to the available number of iron-points in iron oxides.

ABSTRACT

Several studies on the kinetics of reduction of metal oxides have been reported in literature. However, a very important aspect of the oxide reduction which remain to be fully investigated is the morphology and mechanism of nucleation and growth of the metal nuclei on the oxide substrate.

In the present study a mathematical model for the solid state reduction of hematite to wustite by iron is developed to explain the fragmentation of the particles and the porosity generation during topochemical pattern of reduction. Results of the model predictions are confirmed by experimental work.

A model for gaseous reduction is developed in which temperature dependent equivalent rate of iron and oxygen transfer is calculated at 1023K and 1123K. The transformation of hematite to magnetite is found to be controlling step for the overall reduction reaction.

The present work includes microscopic study of the nucleation and growth phenomena during gaseous reduction of the oxides of some FCC metals, including Fe(γ), Ni and Cu. Reduction experiments are performed in one end closed muffle furnace at various temperatures. Nuclei of different metals are observed on the fractured surface of partially reduced samples under scanning electron microscope. During hydrogen reduction of the oxides of Fe(γ), Ni and Cu the metal nuclei grow in the typical shape of a tetrahedral based pyramid. The

growth pattern is correlated to the mixed metal ion transport and oxygen removal control of the reduction reaction as well as to certain crystallographic orientation relationships between the oxide and metal phase. Shape of the iron nuclei (at 1373K) during hydrogen reduction of dicalcium ferrite is also observed to be tetrahedral based pyramid. The habit plane and growth planes for metal nuclei are deduced from the scanning electron micrographs.

The morphological changes associated with the gaseous reduction of oxides of iron and nickel are also studied in detail with the help of scanning electron microscopy and optical microscopy. Severe fragmentation of particles during hematite reduction is observed. Enhanced vertical growth of iron nuclei leads to discontinuities in the iron layer formed on the surface of the parent oxide particle during the very initial stages of both hematite and magnetite reduction with hydrogen at 1423K. At high temperature (1423K) the hematite, magnetite and nickel oxide compacts are found to be reduced topochemically as a whole while at lower temperatures (1273K for magnetite, 1098K for hematite and 823K for nickel oxide) each and every oxide particle starts getting reduced simultaneously throughout the entire cross section. Growth of nickel nuclei as stringers give rise to a morphology typical for nickel oxide reduction at 1423K and eventually these stringers sinter at various points to develop a relatively dense structure.

CHAPTER 1

INTRODUCTION

1.1 Introduction

Reduction of metal oxides is one of the important methods for making metal powder. For example, more than 50% of the total World's production of iron powder is via Hoaganas process which consists of reducing fine iron oxide powder by carbon, followed by grinding and purification of the reduced cake. The morphology of the resulting powder depends upon the temperature of reduction, time of reduction, type of reductant, initial size of the particles etc. Finer powders are produced at low temperatures, while an upper limit for the reduction temperature is imposed by the tendency of the powder to sinter, forming a dense metal layer over the unreduced portion of the particle. This layer prevents the contact of reducing gases with the unreduced portion. The selection of a suitable reducing agent is also very important, and must be made from the standpoint of composition, impurities (especially the H_2O content) and economy of the operation. The reduction process is open to many variations in order to produce a powder with specific properties. One of the advantages of the method is that the morphology of the final powder can be controlled to a certain extent.

Nucleation and growth phenomena play a very important role during the reduction of metallic oxides. But these aspects of the reduction reactions are only partially explored. One can put forward the following reasons for this trend: a) it is very difficult to observe the basic micromechanisms of nucleation; b) there is the obvious pull of the other classical methods like gravimetric etc. where one can get a lot of quantitative data on rates of reduction. It is, therefore, obvious that most researchers have concentrated their efforts on the determination of fractional reduction α vs. time, t , plots for different oxides reduced under different conditions. Only recently there appears to be some shift in emphasis, and researches dealing with the micromechanisms of reduction are receiving greater attention.

In general, a macroscopic parameter such as the mass rate of reduction, $d\alpha/dt$, of crystalline oxide particles is a function of three quantities: the rate of nucleation, rate of growth of nuclei, and the size and shape of the starting particles. The observed α - t plots, in general are the product of the respective influences of the above three quantities. Typical α - t plots for reduction of metallic oxides can be divided into two categories.

The first kind is a sigmoid shaped or the autocatalytic type of plot in which an induction period of considerable

duration is present. This induction period is usually succeeded by an acceleratory period which in turn is followed by a retarding period. This type of plots generally correspond to low and moderate temperature reduction. The second kind exemplifies the reduction behaviour at higher temperatures, where the induction period is virtually absent.

The majority of the reduction reactions that have been investigated to date can be represented by an equation of the type,



where A stands for the oxide phase and C denotes the metallic phase, B is the reducing gas consisting either hydrogen or carbon monoxide or their mixture and D is the product gas.

The onset of Eq. (1) may be regarded as coinciding with the formation of nuclei of metal; these nuclei will appear only after the oxide phase has become sufficiently supersaturated with respect to the metal. The sigmoid shaped α -t plot may be interpreted as arising from the following succession of events: 1) formation of nuclei of metallic phase on the oxide surface, 2) growth of these nuclei at the expense of the parent phase as oxygen is removed at the metal/oxide interface and 3) overlap of the growing nuclei and a decrease in the metal/oxide interface. The induction period in the plot corresponds to the rate of formation of nuclei. In the subsequent acceleration period, $d\alpha/dt$ is

essentially a product of two terms -- one which describes the rate of nucleation and the other the rate of growth of nuclei. If the rate of nucleation is very large, then the entire surface of the oxide specimen becomes rapidly covered with metallic phase and the metal/oxide interface advances inwards at a slower rate. On the other hand, if the rate of nucleation is not large, but the growth of nuclei perpendicular to the surface of the oxide is large, the metal/oxide interface will necessarily be irregular, and the course of the reduction will be determined by the progressive formation of nuclei as the reduction proceeds. The final retarding period corresponds to coalescence of metal nuclei due to sintering effect and difficulty it imposes to the diffusion of the reducing gas. The present work encompasses the nucleation and growth phenomena during the reduction of oxides of some FCC metals, viz. Fe(γ), Ni and Cu.

1.2 Phase Diagrams⁽¹⁾

The following are the phase diagrams for iron -oxygen, nickel-oxygen, copper-oxygen. (Fig. 1.1 - 1.3).

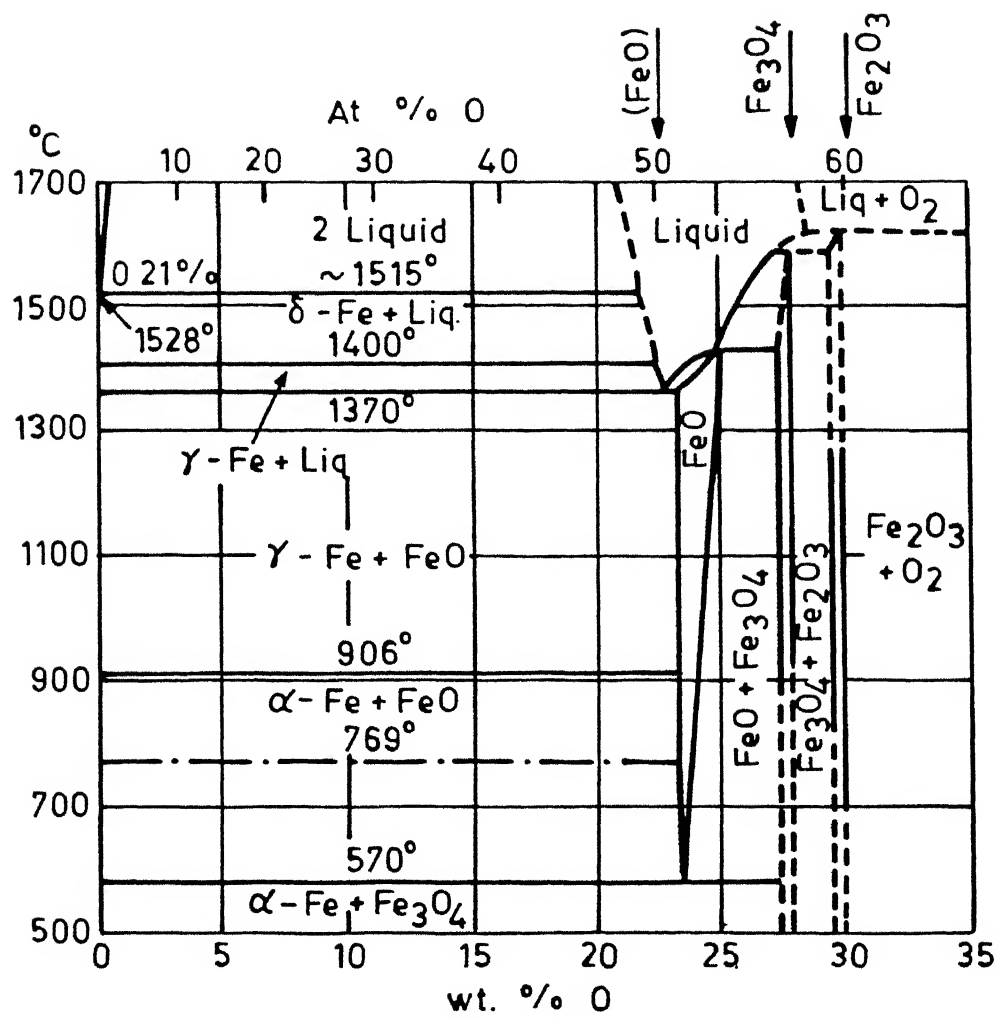


Fig. 1.1. Iron - Oxygen system.

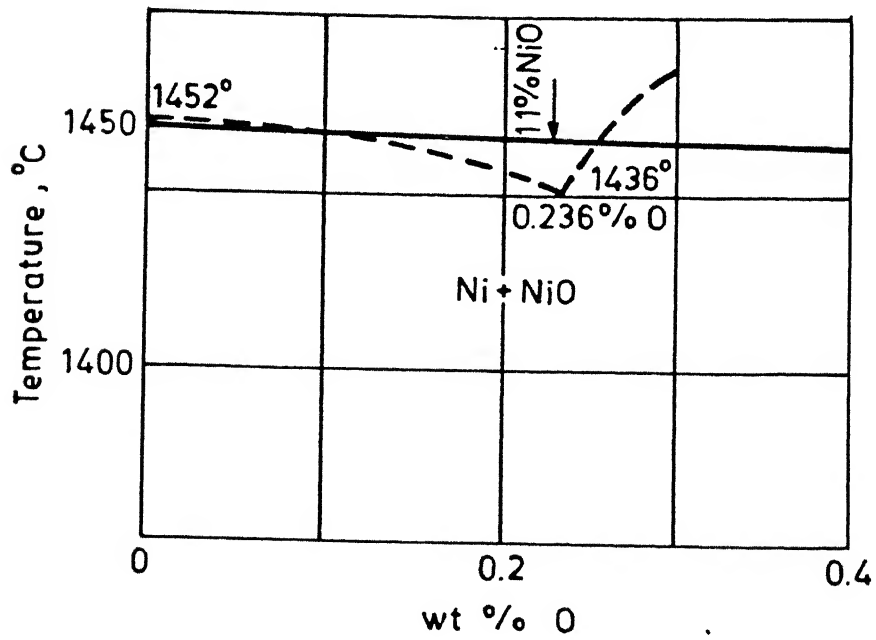


Fig. 1.2. Nickel - Oxygen system.

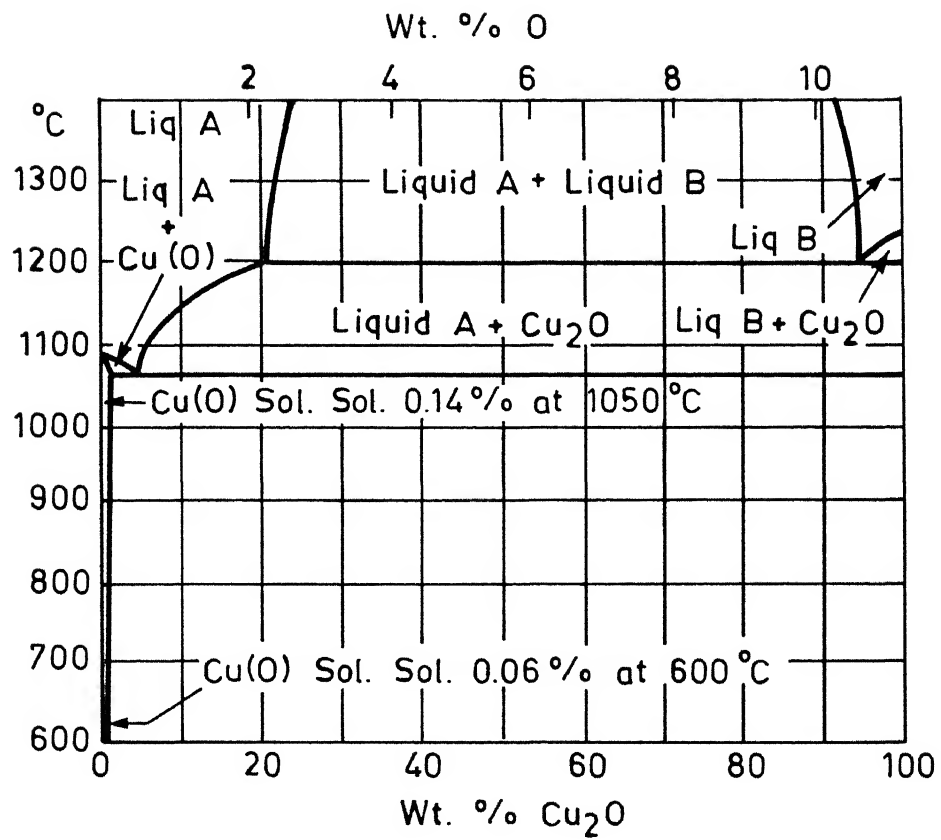


Fig. 1.3. Cu-Cu₂O system.

1.3 Thermodynamic Stability of Iron Oxides⁽²⁾

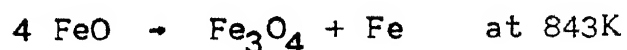
Figure 1.4 shows a general view of the regions of thermodynamic stability of the iron oxides. This is prepared by using the mean values for ΔH , enthalpy change and ΔS , entropy change from the thermodynamic tables. It is observed that hematite and magnetite are stable over a wide range of temperature and oxygen partial pressure, while the stability region of wustite is very narrow. At a higher temperature near 1373K it is 2.5 powers of 10 for the oxygen pressure, then as the temperature decreases it becomes narrower.

1.4 Crystal Structure of FCC Metals and Their Oxides

In our study we are interested in three FCC metals, viz. Iron(γ), Nickel and Copper.

1.4.1 Iron and Its Oxides

It is evident from the iron-oxygen phase diagram, iron and oxygen form three stable oxides viz., Fe_2O_3 (hematite), Fe_3O_4 (magnetite) and FeO (wustite) above 843K while below this temperature wustite phase is unstable. According to Hansen⁽³⁾ considerable uncertainty exists regarding the accurate phase boundaries of wustite with the eutectoid transformation



The crystal structure of hematite can be described as rhombohedrally centred hexagonal lattice⁽⁴⁾ with layers

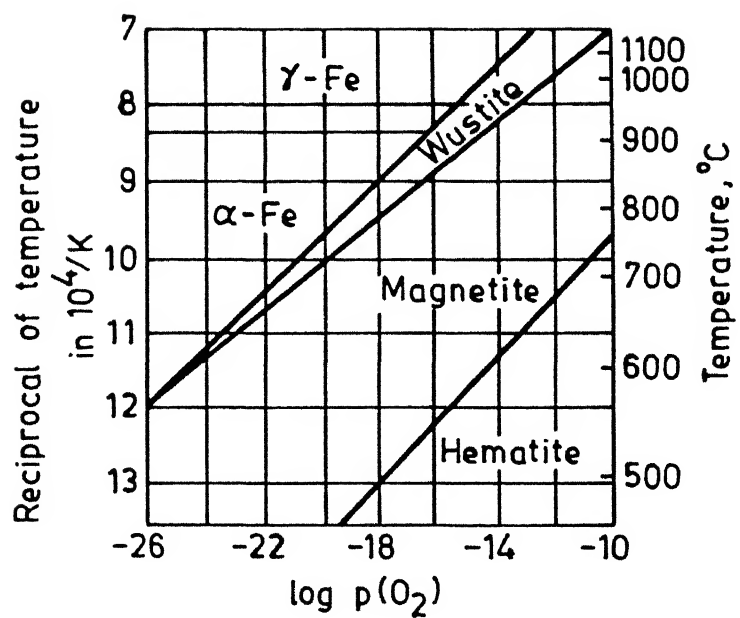


Fig. 1.4. Thermodynamic regions of stability of iron, wustite, magnetite and hematite.

of oxygen ions and layers of iron ions perpendicular to the triad axis. One unit cell of hematite contains 6 formula units (Fe_2O_3). The 18 oxygen ions are arranged in a slightly distorted hexagonal packing while successive cation layers contain equal numbers of iron ions in octahedral coordination.

Magnetite has a cubic lattice with an inverse spinel structure⁽⁵⁾. It can be represented by the formula $\text{Fe}^{3+} \underline{\text{Fe}^{3+}} \underline{\text{Fe}^{2+}}\text{O}_4$. Here the underlined metal ions occupy the octahedral positions. One unit cell contains 8 formula units (Fe_3O_4); 8 ferric ions are tetrahedrally coordinated and 8 ferric and 8 ferrous ions are octahedrally coordinated.

Wustite is a nonstoichiometric oxide in the iron-oxygen system. It, Fe_{1-y}O , may contain between 23.1 and 25.6% oxygen. Wustite crystallizes in the cubic sodium chloride lattice. The oxygen sublattice is largely fully occupied, while on the other hand, a number of lattice points in the iron sub-lattice are vacant. According to Roth⁽⁶⁾ the wustite lattice shows some deviations from the sodium chloride type; his experiments indicated that in some regions of the lattice there is superimposed structure of iron ion vacancies and iron ions in the inter-lattice positions, giving a spinel type structure.

In the formula for wustite Fe_{1-y}O the letter y denotes the proportion of the vacant iron ion lattice positions relative to the available number of iron lattice-points.

The calcium iron pentoxide $\text{Ca}_2\text{Fe}_2\text{O}_5$ (or dicalcium ferrite, $2\text{CaO}, \text{Fe}_2\text{O}_3$) is orthorhombic having the cell dimensions as, $a = 5.428\text{\AA}$; $b = 14.760\text{\AA}$; $c = 5.596\text{\AA}$.

Ferrite ($\alpha\text{-Fe}$) is the low temperature form of iron and it has body centred cubic structure. Above 910°C iron exists in the form of austenite ($\gamma\text{-Fe}$). Its crystal structure is face centred cubic. The temperature range in which mostly_{of} our experiments of hematite and magnetite reduction have been performed, the form of iron is face centred cubic.

Lattice parameters (\AA) for iron and its oxide as functions of temperature $T(^{\circ}\text{C})$ according to Gorton et al.⁽⁷⁾ are,

$$\alpha\text{-Fe} \quad - \quad a = 2.8658 + 3.747 \times 10^{-5}T + 8.59 \times 10^{-9}T^2$$

$$\gamma\text{-Fe} \quad - \quad a = 3.5832 + 7.00 \times 10^{-5}T$$

$$\text{Fe}_{0.924}\text{O} \quad - \quad a = 4.2942 + 6.10 \times 10^{-5}T$$

$$\text{Fe}_3\text{O}_4 \quad - \quad a = 8.3939 + 8.46 \times 10^{-5}T + 5.52 \times 10^{-8}T^2$$

$$\text{Fe}_2\text{O}_3 \quad - \quad a = 5.0298 + 5.30 \times 10^{-5}T + 1.12 \times 10^{-8}T^2$$

$$c = 13.753 + 12.84 \times 10^{-5}T + 1.13 \times 10^{-8}T^2$$

1.4.2 Nickel and Its Oxide

NiO has a sodium chloride type lattice which is inter-penetrating face centred cubic lattice. NiO is a p-type semiconductor.

Upon reduction this NiO is reduced to nickel. It has a face centred cubic lattice.

Lattice parameter of NiO is 4.172 \AA while that of Ni is 3.5239 \AA .

1.4.3 Copper and its Oxides

CuO, has a monoclinic structure

with $a_0 = 4.653 \text{ \AA}$, $b_0 = 3.410 \text{ \AA}$, $c_0 = 5.108 \text{ \AA}$ and α_0 or $\beta_0 = 99^\circ 29'$.

CuO has a simple cubic lattice. Its lattice parameter is 4.2696 \AA .

Cu has a face centred cubic lattice with 3.615 \AA as its lattice parameter.

1.5 Formation of Nuclei and Their Growth

The genesis of both solid and liquid phases is initiated by the formation of nuclei. Volmer et.al.⁽⁸⁾ first gave the theoretical treatment of nuclei-forming processes in 1925 .

The concept of nucleation and subsequent growth is also applicable in metal oxide-metal system. The reduction of metallic oxides commences with the formation of nuclei which are formed on the exposed surfaces of the oxide specimen.

As the metallic oxide surface is exposed to a reducing environment, the oxide loses oxygen which combines with the reducing agent. Now in these places metal/oxygen ratio increases and a gradient is formed, causing the metal to diffuse inwards and vacancies to diffuse outwards. The metal activity goes on increasing at the surface, eventually exceeding the activity of the pure metal (i.e., unity) and a supersaturated region is created below the surface. When the surface activity of metal reaches a critical value, which is high enough locally for nucleation, a critical metal nucleus is formed. This critical nucleus is that volume of the newly formed phase for which the probability of its dissolution is equal to the probability of its further stepwise growth.

Generally, the metallic product and their parent oxide phase differ in their crystal structures. So the formation of an "embryo" results in certain amount of local deformation of the oxide lattice. The difference in molecular volumes of the oxide and metallic phase only adds to the severity of the local deformation.

Reduction potential of the gaseous phase affects the supersaturation of oxide phase with metal concentration. The role of supersaturation in the formation of nuclei in heterogeneous nucleation reactions was discussed by Wagner⁽⁹⁾.

The supersaturation of the oxide phase with respect to metal has ^aconsiderable influence on the kinetics of the reduction

reaction. This is due to the fact that thermodynamic activities of the metal (a_M) and the oxygen (a_O) in the oxide phase having stoichiometric formula M_xO_y are interrelated through the following equation:

$$a_M^x a_O^y = \text{constant} (a_{M_xO_y})$$

where $a_{M_xO_y}$, the activity of M_xO_y , is nearly constant if M_xO_y has a small range of homogeneity. As the supersaturation level rises, the activity of the metal becomes greater than unity whereupon there occurs a corresponding decrease in the activity of oxygen in the bulk oxide phase. But in the neighbourhood of metallic nuclei somewhat different condition prevails; the oxide phase around these nuclei will be depleted of metal and there will be a corresponding increase in the oxygen activity. As a result, the oxygen extraction at the metal oxide/metal/gas three phase boundary is expected to proceed with greater ease.

The number and distribution of the nuclei depends in the first place on the surface structure of the oxide. If it is heterogeneous, nucleation on lattice defects, surface irregularities and inclusions occur. Now for the growth of the nuclei, there must be transport of the metal to the nuclei from the points where oxygen removal occurs. This transportation takes place by means of diffusion of metal ions and electrons through the oxide lattice or along the surface. It is the rate of oxygen removal on one hand and

rate of metal diffusion on the other hand which determine whether in the regions between the originally formed nuclei the supersaturation of metal will be built up which is needed for additional nuclei to form and so increase the density of distribution of the nuclei. The density of distribution, the type and mode of growth of the nuclei, determine the morphology of the metal formed on the oxide, for example nuclei may grow together sidewise to form a covering layer of the new phase which will separate the underlying oxide from the gas phase or the new phase may grow as a sponge on the oxide through the pores of which the gas will have direct access to the original phase or the nuclei may grow rapidly along the perpendicular direction to the surface of the oxide ending up in whiskers. Sometimes combination of all these morphologies may appear at different parts of the oxide during the reduction process.

1.6 Conditions Leading to the Growth of Metal as a Layer or as a Whisker

According to Nicolle and Rist⁽¹¹⁾ the overall reduction process, whatever the stage it has reached, may be divided into two broad mechanisms:

- (i) Oxygen removal, involving transport in the gas phase outside the particle and reaction at the surface.
- (ii) Metal transport in the oxide, based on vacancy diffusion.

The above mechanisms generally operate in series, the former releasing metal ions at the surface and the latter feeding them into the bulk oxide down the metal/oxygen gradient which is formed. However after a nucleus has appeared, in its immediate vicinity, the two mechanisms operate in parallel with the reaction and diffusion simultaneously feeding metal to the growing nucleus.

A variety of situations may develop depending on the relative rates of the mechanisms which are operating. Three cases are examined corresponding to three types of control during the prenucleation stage.

1.6.1 Under Pure Metal Transport Control

In this case the capacity of transport of metal ions from the surface inwards is negligible compared to the capacity of production of such ions at the surface. The metal accumulation is thus restricted to the surface and it would soon reach any degree of supersaturation but for an upper limit defined locally by the critical metal activity for nucleation [Fig. 1.5b]. The site with the lowest critical metal activity thus gives birth to the first metal nucleus. The subsequent growth of this nucleus can take place only via further removal of oxygen around it, since there is no build up of metal to feed the nucleus from the bulk. Diffusion being slow in all directions, the other points on the surface ignore the first nucleus and surface accumulation continues, thus causing nucleation to take place at many other points independently side by side [Fig.1.5c].

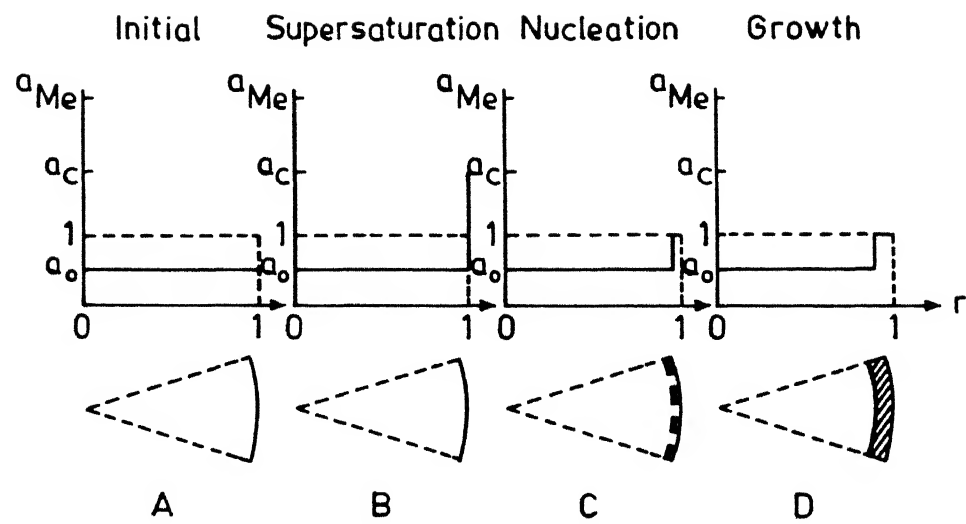


Fig. 1.5. Metal activity curves and phase configuration in a oxide particle when reduced under pure metal transport control.

These nuclei which thus appear to grow radially at their periphery in the shape of plates till they merge to form a layer. This type of growth is quite common and generally they give rise to dense metal layer [Fig. 1.5d].

1.6.2 Under Pure Oxygen Removal Control

In this case the capacity of production of metal ions at the surface is negligible compared to their capacity of transport from the surface inwards to the bulk. The build up of metal thus takes place under a negligible gradient and is practically uniform throughout the volume of the oxide particle, which acts as a reservoir [Fig. 1.6a and b] . The activity of metal increases slowly with time, at a rate which is controlled at the surface. Though nucleation is delayed it occurs eventually at the surface site which has the lowest critical metal activity [Fig. 1.6c]. The first nucleus can grow at the expense of the metal built up in the supersaturated bulk oxide. At the beginning of this process, metal is fed to the nucleus down a very steep gradient, which substantiates the extreme assumption that the rate of the transport mechanism is much higher than that of further reduction. Growth then takes place without any significant removal of oxygen around the nucleus, a condition which leaves it no other possibility than to grow outwards. If the bulk oxide can be depleted quickly enough of its excess metal, a cylindrical whisker is formed [Fig. 1.6d]. Beyond that stage, supersaturation is maintained

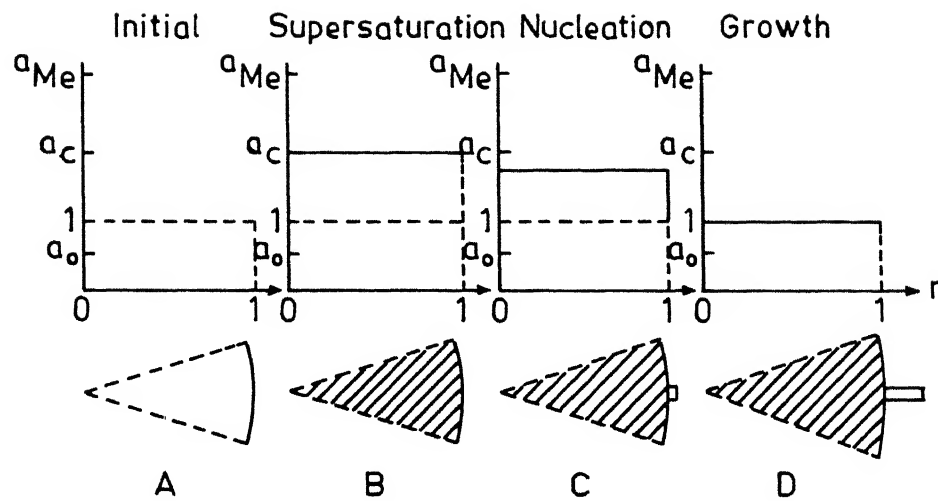


Fig. 1.6. Metal activity curves and phase configuration in a oxide particle when reduced under pure oxygen removal control.

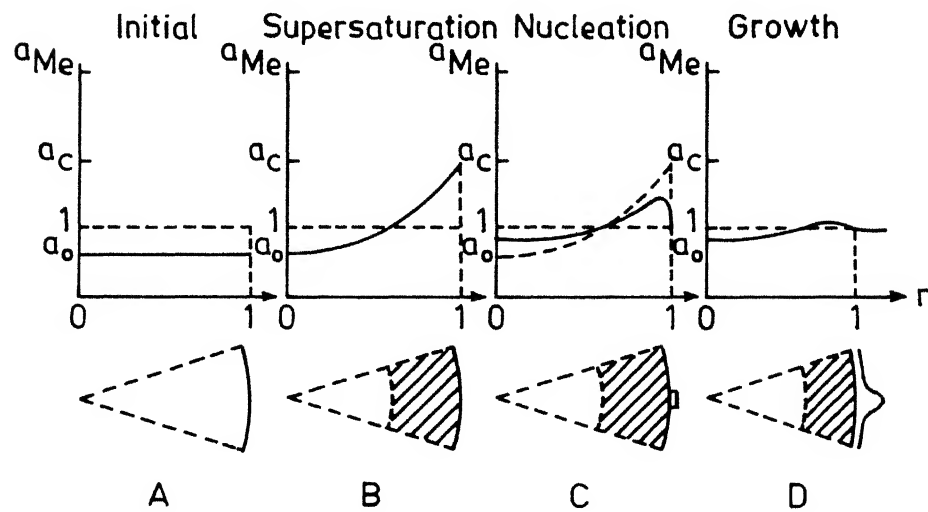


Fig. 1.7. Metal activity curves and phase configuration in a oxide particle when reduced under mixed control.

at a low level by the presence of the new phase acting as a drain and no other nucleus can be formed. The first nucleus remains the only one on the particle.

1.6.3 Under Mixed Control

Here the capacity of production of metal ions at the surface is of the same order of magnitude as their capacity of transport from the surface inwards to the bulk. The build up of metal thus takes place in a limited zone [Fig.1.7b] and the supersaturated region covers up a fraction of the particle volume. The activity of metal at the surface can reach the local critical value at several points over a period of time [Fig. 1.7c] and several nuclei can appear. They can grow from two sources simultaneously: the metal build up in the supersaturated zone and the continuing surface reaction. Oxygen being removed on their sides, the nuclei grow radially as well as outwards and may assume conical shapes [Fig. 1.7d].

1.7 Mechanism and Morphology of Reduction Processes : A Review of Literature

1.7.1 Iron Oxide Reduction

Because of its practical importance, a great deal of work has been done during the past four decades on the gaseous reduction of iron oxides. Some investigators insisted on controlled experimentation on pure material

directed towards the understanding of the mechanism of the reduction process.

Edstrom and Bitsianes⁽¹¹⁾ proposed a gas-solid type of reaction at the iron-wustite phase boundary. Magnetite and hematite at the core were supposed to be reduced to lower oxides by solid state reduction due to inward diffusion of iron from the surface. This mechanism was based on the fact that the wustite lattice contained a high concentration of cationic vacancies through which iron ions could move easily. Warner⁽¹²⁾ put forward mixed chemical and diffusion control mechanism. He demonstrated the importance of diffusion in the reduction of hematite and proposed that both the chemical reaction at the iron-wustite interface and the diffusion through the gas boundary layer and porous product layer are important in the overall rate of reduction .

Turkdogan and Vinters⁽¹³⁾ observed that pore structures of wustite and iron become coarser and pore surface area decreased with increase in temperature. One can attribute this phenomenon to sintering tendency and diffusion predominance of the reaction at higher temperature. Pore structure obtained by carbon monoxide reduction of hematite is coarser than that by hydrogen. They also found that during early stages of reduction ($\sim 30\%$), almost all the hematite and magnetite are converted to wustite.

Kun Li et.al.⁽¹⁴⁾ postulated that if the reduction reaction is purely diffusion controlled then topochemical reaction occurred in a porous specimen. The unreacted core of a theoretically dense particle might recede topochemically if chemical kinetics at the interface control the rate of reduction for a shell of porous product. They also concluded that if the rate of an individual chemical reaction becomes comparable to that of transport through the porous solid, then reaction would occur throughout a finite volume rather than at an interface, and topochemical behaviour would no longer be observed macroscopically.

Bradshaw and Matyas⁽¹⁵⁾, carried out some investigations regarding structural changes and kinetics of gaseous reduction of hematite. They found that reduction of hematite to magnetite was frequently accompanied by the formation of pores which were preserved during subsequent reduction to wustite to iron. The size and distribution of these pores change with variation in reduction temperature, so that the condition under which the magnetite was formed might have a profound effect on its subsequent reduction. They observed that at temperatures below 1073K, the reduction of each hematite grain occurred topochemically and magnetite was porous, while above 1273K growth of magnetite was anisotropic. They concluded that reaction rate was controlled by formation of magnetite nuclei at the hematite - magnetite interface.

According to St. John and Hayes⁽¹⁶⁾, the initial stages of reduction of wustite in pure hydrogen at 1273K and 1373K led to the formation of numerous pits on the oxide surface prior to iron nucleation, but at lower temperatures this phenomena was less pronounced. It was found that the pore sizes produced during reduction increase as the reducing gas composition approaches that of the iron-wustite equilibrium composition. Moukassi et.al.⁽¹⁷⁾ found that at temperatures below 1123K, the iron produced always showed a fine porosity. At temperatures above 1123K, the sintering took place so that dense iron containing big isolated pores were formed. They also pointed out that the evolution of porosity was much more influenced by the reduction temperature than by the reduction rate.

In H_2/H_2O gas mixtures the $\alpha - \gamma$ transition occurs at 1183K. St. John et.al.⁽¹⁸⁾ showed that in relation to the wustite lattice the misfit at the α -Fe/wustite was 5.7%, whereas at the γ -Fe/wustite interface it was 16.4%. Low mismatch in α -Fe tend to give a semicoherent wustite-iron interface, while in case of γ -Fe it should give an incoherent interface. So one can conclude that void formation at the iron wustite interface would be relatively easier at a γ -Fe/wustite interface rather than at an α -Fe/wustite interface.

In a recent investigation by Dube and Deo⁽¹⁹⁾, observations were made during magnetite reduction to wustite to iron at various temperature. They demonstrated that severe pitting and fragmentation took place during solid state reduction of magnetite to wustite by iron, resulting in porous morphology of product iron through which reducing gas had access to unreduced oxide. It was noted that iron nuclei produced on wustite surfaces grew in a typical tetrahedral based pyramid shape till they coalesce to each other. It was also observed that at higher temperatures (1423K) nuclei grew in direction perpendicular to the wustite surface, resulting in whisker in extreme cases while at lower temperatures (1173K) the iron nuclei had a propensity to grow laterally resulting in a dense layer of iron over the wustite surface.

1.7.2 Nickel Oxide Reduction

Both nickel oxide and nickel belong to the cubic type of structure. Incidentally nickel has face centred cubic structure while nickel_{oxide} is having sodium chloride type structures which is interpenetrating face centred cubic structure. So during transformation from oxide to metal lattice distortion involved is not appreciable. According to Cech⁽²⁰⁾ the reduction fronts of growing crystallites of nickel were sometimes oriented parallel to (100) of NiO, sometimes parallel to (110) of NiO and sometimes irregular. More than one

orientation of growing front of reduction crystallites were found on a single specimen of nickel oxide. However no conclusion was drawn regarding ^{the} reduction front orientation on the overall reduction behaviour. He suggested that reduction was accomplished by reaction occurring around structural defects like dislocation where nuclei appeared initially. According to him the reduction rate, which depends on the rate of diffusion of hydrogen through or around the reduction crystallite, should be maximum just after nucleation. Before nucleation the oxide had to become supersaturated with metal till critical nuclei has appeared and then excess metal in the oxide condense over the nucleus and makes it grow.

According to Little et.al.⁽²¹⁾ there are certain stages during nucleation and growth of nickel on nickel oxide. In the initial stages following cubic relationship existed, the $(001)_{\text{NiO}} \parallel (001)_{\text{Ni}}$ and $(111)_{\text{NiO}} \parallel (111)_{\text{Ni}}$ leading to complete matching of the cubic directions and planes in both structures so nickel formed was epitaxial with oxide. Then subsequently majority of nickel nuclei were no longer epitaxial with the oxide as reduction reaction progressed with the appearance of fissures. These fissures might occur due to mismatch between the matrix and the metal nickel particle rotation and loss of coherency may also give rise to fissures. Then, finally nickel nuclei grew and impinged upon each other forming large clusters of nickel metal. During this stage there were complete loss of epitaxy resulting

in well developed pore structure in highly reacted areas.

1.7.3 Copper Oxide Reduction

Veistaro et.al.⁽²²⁾ followed the reduction of cuprous oxide to copper by hot stage scanning electron microscope. They observed nucleation of round copper particles at higher temperatures (1208K) while copper particles were angular at lower reduction temperatures (1068K). At lower temperatures crystal-like shape of the nuclei were visible. One can conclude that in this particular case nuclei grew along certain typical crystal direction and the diffusion within the crystal was not so fast so as to make the nuclei round. However the investigator did not postulate any such crystal directions along which the nuclei growth was most favourable.

Mankhand et.al.⁽²³⁾, studied the behaviour of copper fibre formation during copper sulphide reduction by hydrogen. They postulated the following steps before copper nucleation:

1. The formation of pits and pores in the matrix grain when removal of sulphur began due to condensation of cation vacancies.
2. Nucleation of copper preferentially on these pits as sulphur potential was minimum at those places.

Subsequently, copper ions migrated and condensed on the copper nuclei previously formed in the pits resulting in growth of the nuclei. These investigators did not mention anything about orientation relationship between the growing metal and the sulphide.

In a recent investigation by Bhargava and Dube⁽²⁴⁾, it was found that initially copper emerged at some energetically favourable points on the oxide. Subsequently copper nucleated and grew at more points radially and covered the entire surface. The shape of the nuclei were essentially hemispherical.

1.8 Scope of the Present Work

From the review of literature it becomes evident that nucleation and growth of metal nuclei is important to determine the structural and morphological changes during reduction from their oxides. These changes have a direct bearing on the overall reduction kinetics and nature of the resultant product.

The present work describes the nucleation and growth phenomena during gaseous reduction of oxides of some FCC metals viz. Fe, Ni, Cu. The study includes development of mathematical models for solid state reduction and gaseous reduction of iron oxides. The present work also aims at developing a generalised growth model for iron, nickel and

copper nucleation. Morphological changes taking place at various stages and various temperatures are also investigated during the gaseous reduction of oxides.

CHAPTER 2

EXPERIMENT

2.1 Details of Reduction Chamber

The reduction furnace was made up of two parts. One part being the main reduction chamber, consisted a 800 mm long and 100 mm internal diameter Inconel tube of 6 mm thickness with one end closed. In another part cooling of the samples after reduction was accomplished whose dimension was 350 mm long and it was welded to the main reduction chamber. SiC heating elements were used for heating the reduction chamber in a muffle furnace. It was found that the hot zone of the furnace was 200 mm long, starting from the closed end. A chromel-alumel thermocouple with sheath was put in the hot zone to measure the temperature of that zone. Inside the tubular reduction chamber a rectangular Inconel sheet was inserted for placing the perforated Inconel tray alongwith the samples.

The cylinder gas either nitrogen (used for flushing) or hydrogen (used for reduction), after passing through Lectrodryer⁽²⁵⁾, for moisture absorption, entered respective flowmeters, where volume flow rate of gases were controlled. Then the gas was passed through an Inconel tube of 6 mm internal diameter and was delivered at the reduction zone.

2.2 Raw Materials

In the present study hematite, magnetite, nickel oxide, cupric oxide, iron and copper powders were used.

Hematite concentrate supplied by Ferritas Magneticas of Brazil used for reduction consisted of 98.5 wt% Fe_2O_3 ; 1 wt % SiO_2 ; 0.3 wt % Al_2O_3 and 0.01 wt % P with the following sieve analysis given as mesh number: % retention, 48 : 11; 65:3 ; 100:3; 150:4; 200:9; 270:10; 325:14 and -325 : 45.

Magnetite superconcentrate supplied by L.K.A.B. of Sweden used for reduction was having 71.7 - 71.8 wt % Fe; 0.001 wt % P; 0.003 wt % S; 0.05 - 0.07 wt % CaO; 0.15-0.20 wt % MgO; 0.15 - 0.20 wt % Al_2O_3 and 0.05 - 0.1 wt % SiO_2 . With the following sieve analysis, < 417 μm : 100% ; <208 μm ; 99.9% ; < 104 μm : 96.3% and < 62 μm : 85.3% .

Nickel oxide (AR grade) was of the following sieve analysis, 65:3; 100:6; 150:4; 200:15; 270:18; 325:20 and -325:34.

Cupric oxide (AR grade) was of -242 mesh size.

Pure sponge iron powder (Hoaganas) and pure copper powder was of -100 mesh and -65 mesh respectively.

2.3 Preparation of Compacts

In the present experiment cylindrical compacts of 18 mm diameter, 5 mm thickness and approximately 40% porosity were

prepared. Theoretical density values of different oxides were gathered, and mass of powder required for maintaining 60% of theoretical density was computed for individual oxides. Then compacts were made at different pressures in the press. Density was plotted against the pressure. From this plot the actual pressure requirement for particular density was obtained and applied. In the present study the pressure applied ranges from 850 MN/m^2 - 950 MN/m^2 . Zinc stearate was used as lubricant in die during the compact preparation. For making hematite compacts a few drops of water were added to the powder as a binder just before compaction.

2.4 Sintering and Reduction of Compacts

At first the reduction chamber was heated gradually to the desired temperature. Then the reduction chamber was flushed with nitrogen. For reduction experiments hydrogen was passed in the reduction chamber after sufficient flushing was achieved. The unused reducing gas was burnt at the exit end of the reduction chamber.

The required gas was allowed to pass through the reduction chamber which was kept at the required temperature. The compacts were placed on a perforated Inconel tray and were then transferred carefully into the hot zone of the furnace in order to avoid thermal cracking. After reduction

the tray alongwith the compacts was pulled out from furnace into the cooling box, while maintaining a neutral atmosphere of nitrogen. After allowing the compacts to cool down for say 10 mins. in the cooling chamber, they were taken out of the chamber.

The hematite and magnetite compacts were partially reduced by hydrogen for 180-360s in the range of temperature 1068-1423K and 1273-1423K respectively. Pure iron powder (-100 mesh) was added to hematite in 100% excess of the stoichiometric requirement to produce magnetite by heating in nitrogen at 823K for 16 hours. In a similar experiment pure calcium carbonate was added to hematite in 100% excess of the stoichiometric requirement to produce dicalcium ferrite $2\text{CaO} \cdot \text{Fe}_2\text{O}_3$ by heating in nitrogen at 1373K for 4 hours and the sintered compact was then partially reduced by hydrogen for 180-360s at 1373K.

Nickel oxide compacts were partially reduced in hydrogen for 180-360s at 873K and 1423K.

Pure copper powder (-65 mesh) was added to cupric oxide in 100% excess of the stoichiometric requirement to produce cuprous oxide (Cu_2O) by heating in nitrogen at 873K for 4 hours. Cu_2O was then partially reduced in hydrogen for 180-300s at 873K.

For all experiments the linear velocity of hydrogen gas flow was 0.021 m/s.

2.5 Specimen Preparation for Observation under SEM and Optical Microscope

After the reduction the cylindrical samples were fractured across the thickness direction as shown in Fig. 2.1a.

Then for SEM observation one part was gold coated on its fracture surface (Fig. 2.1b). This surface was observed directly under SEM from the edge to the centre which revealed the morphology of products at various stages of reduction.

For optical microscopy the specimens were impregnated with araldite and then cured. The impregnated sample was cold mounted and polished before observing under optical microscope.

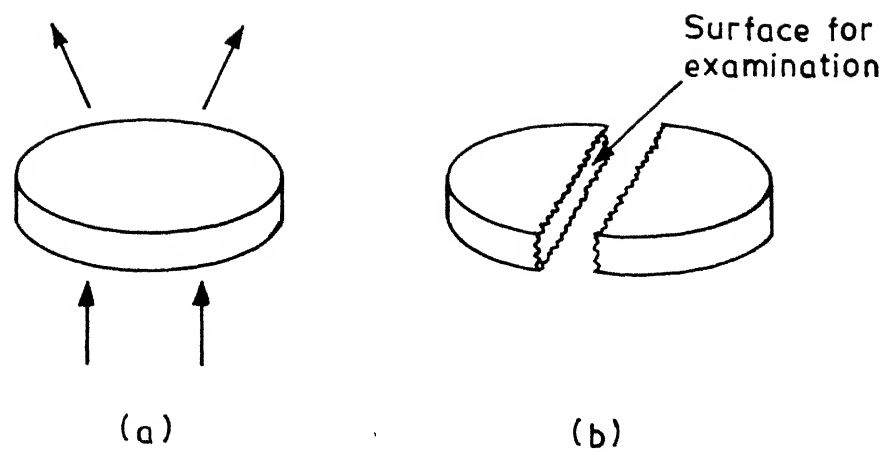
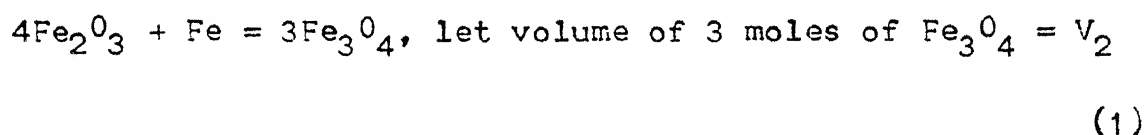


Fig. 2.1. Specimen preparation.

CHAPTER 3

RESULTS AND DISCUSSION3.1 SOLID STATE REDUCTION OF HEMATITE AND MAGNETITE3.1.1 The Model

In the solid state reduction of Fe_2O_3 by metallic iron the ultimate product is Fe_{1-y}O but an intermediate layer of Fe_3O_4 is expected to form at $\text{Fe}_2\text{O}_3/\text{Fe}_3\text{O}_4$ interface according to:



Similarly, at $\text{Fe}_{1-y}\text{O}-\text{Fe}_3\text{O}_4$ interface, a unit quantity of metal will transform Fe_3O_4 as,



let volume of 4 moles of $\text{FeO} = V_1$.

The fluxes of Fe through FeO and Fe_3O_4 , are given respectively by J and $(1-\alpha) J$ where,

$$J = \frac{K_1}{X_1} ; (1-\alpha) J = \frac{K_2}{X_2} \quad (3)$$

$(1-\alpha)$ is the fraction of iron ion ultimately arriving at $\text{Fe}_3\text{O}_4/\text{Fe}_2\text{O}_3$, X_1 and X_2 are thickness of product layers, K_1 and K_2 are constants to be evaluated from diffusion and oxygen potential gradients. The growth rate of FeO and Fe_3O_4

layers are given by

$$\frac{dX_1}{dt} = \alpha J V_1; \quad \frac{dX_2}{dt} = (1-\alpha) J V_2 - J V_1 \quad (4)$$

From equation (3) the value of α can be obtained as -

$$\alpha = \frac{K_1 X_2 - K_2 X_1}{X_2 K_1} \quad (5)$$

Substituting the values of α and J in equation (4),

$$\frac{dX_1}{dt} = V_1 \left(\frac{K_1}{X_1} - \frac{K_2}{X_2} \right) \quad (6)$$

$$\frac{dX_2}{dt} = \frac{K_2}{X_2} (V_1 + V_2) - \frac{K_1}{X_1} V_1 \quad (7)$$

From equation (6), for $\frac{dX_1}{dt}$ to be positive, $\frac{K_1}{X_1} > \frac{K_2}{X_2}$ (8)

Similarly, from equation (7), for $\frac{dX_2}{dt}$ to be positive,

$$\frac{K_2}{X_2} (V_1 + V_2) > \frac{K_1}{X_1} \cdot V_1$$

or

$$\frac{K_2}{X_2} \cdot \frac{X_1}{K_1} > \frac{1}{\left(1 + \frac{V_2}{V_1}\right)} \quad (9)$$

cc/3mole

In the case of magnetite $V_2 = 134.1$ and for wustite $V_1 = 47.6$ cc/4mole. During the initial stages of solid state reduction of hematite by iron the magnetite must form and therefore condition (9) will hold good. The ratio (GR) of growth rates of magnetite and

wustite is given by,

$$GR = \frac{\frac{K_2}{X_2} (V_1 + V_2) - \frac{K_1}{X_1} V_1}{V_1 \left(\frac{K_1}{X_1} - \frac{K_2}{X_2} \right)} \quad (10)$$

On multiplying both the numerator and the denominator by $\frac{X_1}{K_1 V_1}$ in equation (10),

$$GR = \frac{\frac{K_2}{X_2} \cdot \frac{X_1}{K_1} \left(1 + \frac{V_2}{V_1} \right) - 1}{\left(1 - \frac{K_2}{X_2} \cdot \frac{X_1}{K_1} \right)} \quad (11)$$

In the initial stages of reduction the essential condition for Fe_3O_4 to form and grow on Fe_2O_3 in preference to FeO is that $GR > 1$. Since $K_2 X_1 / X_2 K_1$ is less than 1, the ratio V_2/V_1 can be made larger by a factor 'f' such that -

$$\frac{K_2 X_1 / X_2 K_1 (1 + f \cdot V_2/V_1) - 1}{(1 - K_2 X_1 / X_2 K_1)} > 1 \quad (12)$$

putting $t = K_2 X_1 / X_2 K_1$, one obtains,

$$(t + t \cdot f \cdot V_2/V_1 - 1) > (1-t) \quad (13)$$

$$\text{or} \quad f > \left(\frac{2}{t} - 2 \right) \cdot V_1/V_2 \quad (14)$$

From equation (9) the minimum value of 't' for positive growth rate of magnetite is-

$$t > \frac{1}{(1 + V_2/V_1)} \quad (15)$$

Substituting in equation (14) yields-

$$f > 2 \quad (16)$$

Thus if the layers of Fe_3O_4 and FeO are to form on hematite (topochemical reduction patterns) it must be accompanied by an increase in the ratio V_2/V_1 by factor $f > 2$. This increase can occur only if magnetite formed is porous. Though it was experimentally observed by many workers in the past that a large surface area due to cracks etc. was created in the formation of magnetite on Fe_2O_3 and therefore the reduction of hematite proceeded more rapidly than that of magnetite, no mathematical proof of this phenomena was provided as shown above in equation (16). The suggestions put forward earlier were only qualitative viz.

- (a) lattice of Fe_2O_3 differs appreciably from that of magnetite and therefore due to transformation stresses reduction product with greater porosity were formed, or
- (b) cracks are formed due to dependence of morphology on temperature etc.

3.1.2 Application of the Model to the Experimental Data

- (a) Solid state transformation of Fe_2O_3 to Fe_3O_4

One can consider the condition for which iron is transferred at the hematite-magnetite phase boundary. If 'J' is the number of moles of iron transfer per unit area of the phase boundary, one can write⁽²⁶⁾ the expression:

$$J = \frac{D(\text{Fe in Fe}_3\text{O}_4)t}{2V_{\text{Fe}_3\text{O}_4} s_{\text{Fe}_3\text{O}_4}} [\log p(\text{O}_2)_{\text{Fe}_2\text{O}_3/\text{Fe}_3\text{O}_4} - \log p(\text{O}_2)_{\text{Fe}_3\text{O}_4/\text{FeO}}] \quad (17)$$

where,

$$\begin{aligned} D(\text{Fe in Fe}_3\text{O}_4) &= \text{Diffusion coefficient of Fe in Fe}_3\text{O}_4 \\ &= 5.2 \exp \left[- \frac{55000}{RT} \right] \end{aligned}$$

$$\begin{aligned} V_{\text{Fe}_3\text{O}_4} &= \text{Molar volume of Fe}_3\text{O}_4 \\ &= 44.7 \text{ cc mole}^{-1} \end{aligned}$$

$$s_{\text{Fe}_3\text{O}_4} = \text{thickness of magnetite layer}$$

$$t = \text{time for required thickness of the magnetite layer}$$

$$\log p(\text{O}_2)_{\text{Fe}_2\text{O}_3} \text{ or } \log p(\text{O}_2)_{\text{Fe}_3\text{O}_4/\text{FeO}} = \text{logarithm of particle pressure of oxygen at the concerned phase boundary}$$

One can write from (17).

$$t = \frac{2J' V_{\text{Fe}_3\text{O}_4} s_{\text{Fe}_3\text{O}_4}}{D(\text{Fe in Fe}_3\text{O}_4) [\log p(\text{O}_2)_{\text{Fe}_2\text{O}_3/\text{Fe}_3\text{O}_4} - \log p(\text{O}_2)_{\text{Fe}_3\text{O}_4/\text{FeO}}]} \quad (18)$$

For production of 1.0×10^{-7} mole of Fe_3O_4 , 0.33×10^{-7} mole of iron is needed per unit area of the phase boundary and assuming the thickness of magnetite layer formed as 0.005 cm, the time requirement at 823K is,

$$t \sim 1.42 \times 10^2 \text{ hours} \quad (19)$$

In the present study iron was added to hematite with 100% excess of the stoichiometric amount to obtain magnetite according to equation (1). A compact of this mixture was heated at 823K in the neutral atmosphere of nitrogen for 16 hours. It is evident from figure 3.1 and 3.2 that apparently there was no change in the structure and the morphology remains more or less the same before and after the reduction. It appears that there was hardly any transformation of hematite to magnetite. This was expected as it is evident from equation (19) that the time of the reduction of hematite to magnetite in our experiment was very low so that the possibility of magnetite formation was almost negligible.

(b) Solid State Transformation of Fe_3O_4 to FeO

It was until, recently, assumed that since the molal volumes of Fe_3O_4 and FeO relative to equal oxygen content were approximately same the transformation of Fe_3O_4 to FeO was expected to result in formation of dense layer of FeO on Fe_3O_4 , free from cracks and pore. However Dube and Deo (19) have shown that during the solid state reduction of Fe_3O_4 to FeO by iron considerable slitting and fragmentation of magnetite particles occurred. It was observed in their study that porosity created in the step Fe_3O_4 to FeO was approximately 20 percent and hence the factor 'f' in equation (16) should be increased by the same amount for hematite reduction, i.e.,

$$f > 2.5 \quad (20)$$

The genesis of porosity creation in the reduction step FeO to Fe is discussed separately in the section 3.4.

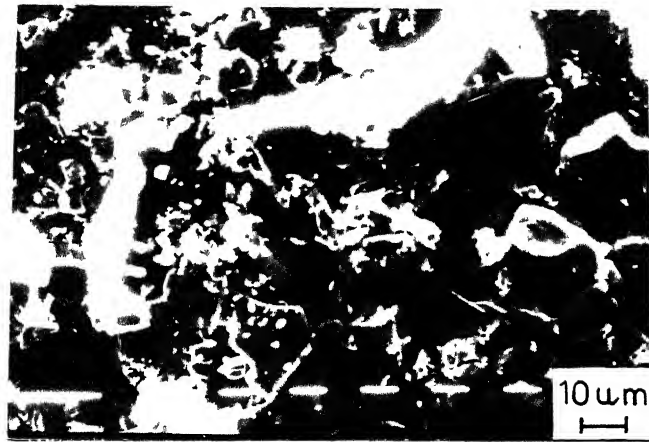


Fig. 3.1 : SEM of mixed hematite and iron compact to produce magnetite by solid state reduction.



Fig. 3.2 : SEM of the same compact as in Fig. 3.1 after heating in nitrogen at 823K for 16 hours.

3.2 MATHEMATICAL MODEL FOR GASESOUS REDUCTION OF IRON OXIDE

3.2.1 Introduction

During reduction of Fe_2O_3 to iron at temperatures above 823K, two more intermediate oxides, i.e. Fe_3O_4 and FeO are formed. At the phase boundaries of these oxides phase transformations as well as transfer of ions, electrons, and vacancies occur. In this work a model is developed for the first time for reduction of iron oxide (i.e., Fe_2O_3) by hydrogen by taking into account structural elements of disorder, deviation from stoichiometry and phase boundary reactions. Earlier a similar attempt has been made by Schwenk and Rahmel⁽²⁷⁾ for the oxidation of iron.

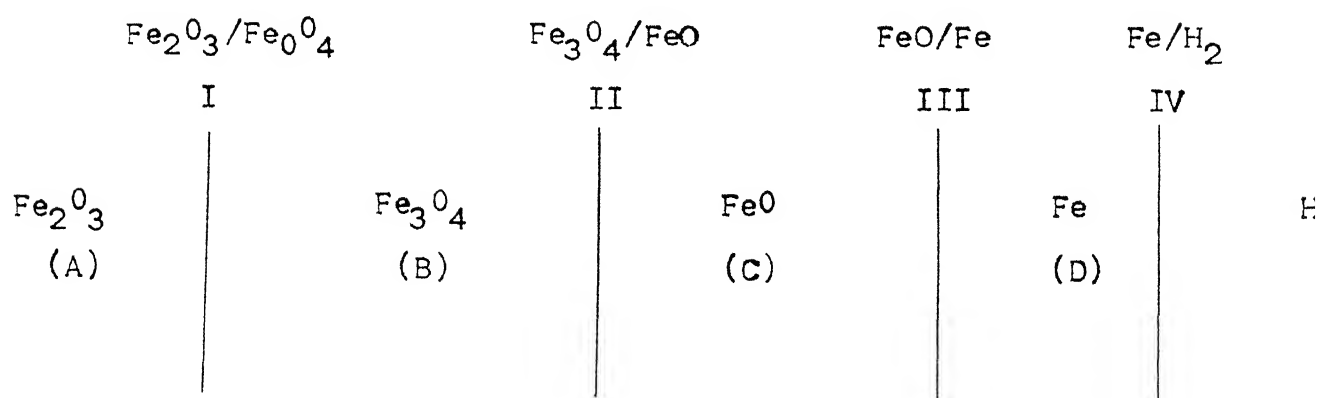
3.2.2 Summary of Defects and Deviation from Stoichiometry

The defects and deviation from stoichiometry in the three oxides of iron can be summarised as follows:

	Fe_2O_3	Fe_3O_4	FeO
Structural elements of disorder	$V_{\text{O}}^{\bullet\bullet}, \text{Fe}_i^{\bullet\bullet}; e'$	$V_{\text{Fe}}'', V_{\text{Fe}}''', h^{\bullet}$	V_{Fe}''
Deviation from stoichiometry	$\text{Fe}_{2(1+z)}\text{O}_{3(1-u)}$	$\text{Fe}_{3(1-x)}\text{O}_4$	$\text{Fe}_{(1-y)}\text{O}$

where,

V_{Fe}'' & V_{Fe}''' = negatively charged iron vacancies
 $V_O^{\bullet\bullet}$ = positively charged oxygen vacancies
 $Fe_i^{\bullet\bullet}$ = positively charged interstitial iron ions
 h^\bullet = positively charged hole
 e' = free electron
 V_i = unoccupied interstitial position



Different phases and phase boundaries.

3.2.3 Phases and Phase Boundaries to be Considered during Reduction

The phases and phase boundaries created during reduction are as follows:

Let the phase boundaries be designated as,

$$Fe_2O_3/Fe_3O_4 = I; Fe_3O_4/FeO = II; FeO/Fe = III; Fe/H_2 = IV$$

and phases be designated as,

$$Fe_2O_3 = A; Fe_3O_4 = B; FeO = C; Fe = D.$$

The following simplifying assumptions are made in the model.

1. The oxide phases, i.e. Fe_2O_3 , Fe_3O_4 , FeO are homogeneous.
2. The Fe/O ratios and the hydrogen pressures are constant at the phase boundaries I, II, III, IV.
3. The species involved in matter transport (ions, electrons, vacancies, are assumed to be

In A : $V_{\text{O}}^{\bullet\bullet}$, $\text{Fe}_i^{\bullet\bullet\bullet}$ and e' from I to II

In B : V_{Fe}'' , V_{Fe}''' and h^\bullet from II to III

In C : V_{Fe}'' and h^\bullet from III to IV.

4. Phase transformations and mass transfer across the phase boundaries for maintaining the local Fe/O ratios are:

At I : Transport of oxygen vacancies from A to B.

Transformations of Fe_2O_3 to Fe_3O_4

At II : Transport of Fe vacancies from B to C.

Transformation of Fe_3O_4 to FeO

At III: Transport of Fe vacancies from C to D

Transformation of FeO to Fe .

With these assumptions phase boundary reaction equations can be written as follows:

<u>Boundary</u>	<u>Rate</u>	<u>Reaction Equation</u>	<u>Reaction</u>
I	i_1	$\text{Fe}_2\text{O}_3 + \text{H}_2 \rightarrow \text{H}_2\text{O} + [V_{\text{O}}^{\bullet\bullet} + 2e' + 2\text{Fe}_{\text{Fe}}^x + 2\text{O}_{\text{O}}^x]_{\text{A}}$	(1)
I	i_2	$\text{Fe}_2\text{O}_3 + 2(V_i)_{\text{A}} \rightarrow 2(\text{Fe}_i^{\bullet\bullet\bullet} + 3e')_{\text{A}} + 3\text{O}_{\text{O}}^x$	(2)

<u>Boundary</u>	<u>Rate</u>	<u>Reaction Equation</u>	<u>Reaction</u>
I	i_3	$2\text{Fe}_2\text{O}_3 + [2\text{Fe}_{\text{Fe}}^{\text{x}} + \text{V}_{\text{O}}^{\bullet\bullet} + 2\text{e}' + 3\text{O}_{\text{O}}^{\text{x}}]_{\text{A}} + \text{H}_2$ $\rightarrow 2\text{Fe}_3\text{O}_4 + \text{H}_2\text{O}$	(3)
I	i_4	$4\text{Fe}_2\text{O}_3 + [\text{Fe}_{\text{Fe}}^{\bullet\bullet\bullet} + 3\text{e}']_{\text{A}} \rightarrow 3\text{Fe}_3\text{O}_4 + (\text{V}_{\text{Fe}})_{\text{A}}$	(4)
I	i_5	$5\text{Fe}_3\text{O}_4 + [\text{V}_{\text{Fe}}^{\prime\prime} + \text{V}_{\text{Fe}}^{\prime\prime\prime} + 5\text{h}^{\bullet} + \text{Fe}_{\text{Fe}}^{\text{x}} + 4\text{O}_{\text{O}}^{\text{x}}]_{\text{B}}$ $\rightarrow 8\text{Fe}_2\text{O}_3$	(5)
II	i_6	$\text{Fe}_3\text{O}_4 + [2\text{V}_{\text{Fe}}^{\prime\prime} + 4\text{h}^{\bullet}]_{\text{C}} \rightarrow 2\text{FeO} +$ $[\text{V}_{\text{Fe}}^{\prime\prime} + \text{V}_{\text{Fe}}^{\prime\prime\prime} + 5\text{h}^{\bullet} + \text{Fe}_{\text{Fe}}^{\text{x}} + 2\text{O}_{\text{O}}^{\text{x}}]_{\text{B}}$	(6)
II	i_7	$\text{Fe}_3\text{O}_4 + \text{H}_2 \rightarrow 3\text{FeO} + (\text{V}_{\text{Fe}}^{\prime\prime} + 2\text{h}^{\bullet})_{\text{C}} + \text{H}_2\text{O}$	(7)
III	i_8	$\text{FeO} + [\text{V}_{\text{Fe}}^{\prime\prime} + 2\text{h}^{\bullet}]_{\text{C}} + \text{H}_2 \rightarrow \text{Fe} + \text{H}_2\text{O}$	(8)

The above reaction equations are balanced with respect to mass, charge and lattice sites and for the sake of balancing only complete unit cells are considered.

The above eight reactions contribute to the growth of different phases in the following way:

<u>Boundary</u>	<u>Reaction</u>	<u>Fe_2O_3</u>	<u>Fe_3O_4</u>	<u>FeO</u>	<u>Fe</u>
I	(1)	$-i_1 + i_1$			
I	(2)	$-i_2$			
I	(3)	$-3i_3$	$+2i_3$		
I	(4)	$-4i_4$	$+3i_4$		

<u>Boundary</u>	<u>Reaction</u>	<u>Fe₂O₃</u>	<u>Fe₃O₄</u>	<u>FeO</u>	<u>Fe</u>
I	(5)	+8i ₅	-6i ₅		
II	(6)		+i ₆ -i ₆	-2i ₆ +2i ₆	
II	(7)		-i ₇	+4i ₇	
III	(8)			-2i ₈	+i ₈

In the above case the rates of phase growth are balanced. Negative signs mark the number of unit cells of the phase at the left hand side and positive signs the number of unit cells at the right hand side of the corresponding equations.

For the growth rates of the oxide phases, it would be clear that

$$I_A = -i_2 - 3i_3 - 4i_4 + 8i_5 \quad (9)$$

$$I_B = 2i_3 + 3i_4 - (6i_5 + i_7) \quad (10)$$

$$I_C = 4i_7 - 2i_8 \quad (11)$$

$$I_D = i_8 \quad (12)$$

3.2.4 Balance of Defects

Defects are formed and/or consumed at the different phase boundaries as follows:

<u>Element of disorder</u>	<u>Formation</u> <u>Boundary/Rate</u>		<u>Consumption</u> <u>Boundary/Rate</u>	
$(V_O^{\bullet\bullet} + 2e')$	I	i_1	I	i_3
$(Fe_i^{\bullet\bullet} + 3e')$	I	$2i_2$	I	i_4
$(V_{Fe}'' + V_{Fe}'' + 5h^{\bullet})$	II	i_6	I	i_5
$(V_{Fe}'' + 2h^{\bullet})$	II	i_7	II & III	$2i_6 + i_8$

If the population of each defect remains nearly constant, then following equations can be obtained,

$$i_1 = i_3 \quad (13)$$

$$2i_2 = i_4 \quad (14)$$

$$i_5 = i_6 \quad (15)$$

$$i_7 = 2i_6 + i_8 \quad (16)$$

3.2.5 Calculation of Growth Rates

From equations (9) - (12) and (13) - (16) one gets

$$I_A = 8i_6 - 4.5i_4 - 3i_3 \quad (17)$$

$$I_B = 2i_3 + 3i_4 - (8i_6 + i_8) \quad (18)$$

$$I_C = 8i_6 + 2i_8 \quad (19)$$

The expression for growth rate of Fe-equivalent and Oxygen-equivalent can be written as,

$$\begin{aligned}
 I_{Fe} &= 3I_B + I_C \\
 &= 6i_3 + 9i_4 - 16i_6 - i_8
 \end{aligned} \tag{20}$$

and

$$I_O = 3I_A + 4I_B + I_C = -(2i_8 + 1.5i_4 + i_3) \tag{21}$$

I_{Fe} and I_O signifies the rate of iron and oxygen transfer respectively through different phase boundaries in opposite directions.

If one makes an assumption that the layers of different oxide phases reduce orthogonally then it follows that the layer thickness, the number of unit cells and their changes are mutually proportional. The layer thickness of a particular phase can be expressed as the number of unit cells per unit area multiplied by the molar volume of that particular phase. Based on this one can derive the following relationship⁽²⁷⁾:

$$P = \frac{I_A}{I_B} = (s_{Fe_2O_3}/s_{Fe_3O_4}) \times (V_{Fe_3O_4}/V_{Fe_2O_3}) \tag{22}$$

and

$$R = \frac{I_B}{I_C} = (s_{Fe_3O_4}/s_{FeO}) \times (V_{FeO}/V_{Fe_3O_4}) \tag{23}$$

where,

s_{oxide} = layer thickness of oxide phase;

V_{oxide} = molar volume of oxide.

Now from equations (17), (18), (19), (22) and (23) one gets,

$$P = \frac{8i_6 - 4.5i_4 - 3i_3}{2i_3 + 3i_4 - (8i_6 + i_8)} \quad (24)$$

$$R = \frac{2i_3 + 3i_4 - (8i_6 + i_8)}{8i_6 + 2i_8} \quad (25)$$

Since,

$$I_{Fe} = 3I_B + I_C$$

and

$$I_O = 3I_A + 4I_B + I_C$$

from equations (22) and (23) one gets

$$P = I_A/I_B, \text{ so } I_A = PI_B$$

and

$$R = I_B/I_C, \text{ so } I_B = RI_C \quad (26)$$

hence,

$$I_A = PR I_C. \quad (27)$$

Thus,

$$I_{Fe} = 3RI_C + I_C = I_C (3R + 1) \quad (28)$$

and

$$I_O = 3PRI_C + 4RI_C + I_C = I_C (3PR + 4R + 1) \quad (29)$$

It is clear that from an actual experiment the value of P and R can be obtained by measuring the value of layer thickness and I_C can be calculated to obtain the

the value of I_{Fe} and I_O from equations (28) and (29) respectively.

I_C is related to i_6 and i_8 which are the rate of movements of movement of iron in Fe_3O_4 and FeO respectively.

The expressions for i_6 and i_8 can be written (26) as,

$$i_6 = \frac{D(Fe \text{ in } Fe_3O_4)}{2V_M \cdot s_{Fe_3O_4}} \left[\log p(O_2)_{Fe_2O_3/Fe_3O_4} - \log p(O_2)_{Fe_3O_4/FeO} \right] \quad (30)$$

$$i_8 = \frac{D(Fe \text{ in } FeO)}{2V_M \cdot s_{FeO}} \left[\log p(O_2)_{Fe_3O_4/FeO} - \log p(O_2)_{FeO/Fe} \right] \quad (31)$$

where,

$$\begin{aligned} D(Fe \text{ in } Fe_3O_4) &= \text{Diffusion coefficient of Fe in } Fe_3O_4 \\ &= 5.2 \exp(-55000/RT) \end{aligned}$$

$$\begin{aligned} D(Fe \text{ in } FeO) &= \text{Diffusion coefficient of Fe in FeO} \\ &= 4.5 \times 10^{-2} \times y \exp(-27000/RT) \end{aligned}$$

$$y = \text{nonstoichiometric factor for FeO. It depends on temperature}$$

$$\begin{aligned} V_M &= \text{molar volume of the oxide phase concerned} \\ V_{Fe_2O_3} &= 30.4 \text{ cc mole}^{-1} \\ V_{Fe_3O_4} &= 44.7 \text{ cc mole}^{-1} \\ V_{FeO} &= 12.2 \text{ cc mole}^{-1} \end{aligned}$$

3.2.6 Application of Model to Experimental Data

Bitsianes and Joseph⁽²⁸⁾ carried out some experiments on reduction of Fe_2O_3 by hydrogen at 1023K and 1123K and observed that the layers of iron oxides formed topochemically. On a macroscale, the layers of various oxides appeared to be sharply defined. From their experiment,

$$s_{\text{FeO}}^{1023} = 0.055 \text{ cm}; \quad s_{\text{Fe}_3\text{O}_4}^{1023} = 0.008 \text{ cm}; \quad s_{\text{Fe}_2\text{O}_3}^{1023} = 0.255 \text{ cm}.$$

$$s_{\text{FeO}}^{1123} = 0.077 \text{ cm}; \quad s_{\text{Fe}_3\text{O}_4}^{1123} = 0.006 \text{ cm}; \quad s_{\text{Fe}_2\text{O}_3}^{1123} = 0.377 \text{ cm}.$$

One can now calculate i_6 and i_8 at 1023K and 1123K by Fig. 1.4, equations (30) and (31) respectively.

$$i_6^{1023} = 1.0489 \times 10^{-10} \text{ mole/cm}^2/\text{sec}.$$

$$i_8^{1023} = 2.732 \times 10^{-9} \text{ mole/cm}^2/\text{sec}.$$

$$i_6^{1123} = 1.423 \times 10^{-9} \text{ mole/cm}^2/\text{sec}.$$

$$i_8^{1123} = 2.491 \times 10^{-5} \text{ mole/cm}^2/\text{sec}.$$

Putting the values of i_6 and i_8 at 1023K and 1123K in (19) one obtains

$$I_C^{1023} = 6.303 \times 10^{-9} \text{ mole/cm}^2/\text{sec}.$$

and

$$I_C^{1123} = 4.984 \times 10^{-5} \text{ mole/cm}^2/\text{sec}.$$

A104133

One can calculate P and R values at 1023K and 1123K from the given data as,

<u>Temp. °K</u>	<u>P</u>	<u>R</u>
1023	42.23	0.0437
1123	83.23	0.0234

So according to equations (28) and (29)

$$I_{Fe}^{1023} = 7.129 \times 10^{-9} \text{ mole/cm}^2/\text{sec.}$$

$$I_{Fe}^{1123} = 5.333 \times 10^{-5} \text{ mole/cm}^2/\text{sec.}$$

$$I_O^{1023} = 4.234 \times 10^{-8} \text{ mole/cm}^2/\text{sec.}$$

and

$$I_O^{1123} = 3.462 \times 10^{-4} \text{ mole/cm}^2/\text{sec.}$$

3.2.7 Discussion

I_{Fe} and I_O are equivalent rates of transfer of iron and oxygen respectively through different phase boundaries. In the example given above I_{Fe} and I_O were calculated at 1023K and 1123K. It is clear that both I_{Fe} and I_O increase with temperature. At higher temperatures structural disorder increases and hence lattice defects, metal ions etc. diffuses faster, which, in turn, increases the kinetics of the process. One can perform the reduction reaction at different temperatures under a given set of conditions from where one can get the thicknesses of different oxide layers and compute I_{Fe} and I_O

values at different temperatures. I_{Fe} and I_O can be plotted as a function of temperature and from there one can derive equations for the dependence of I_{Fe} and I_O on temperature.

It may however be noted that both I_{Fe} and I_O depend on the amount of porosity present in different phases. Thus the type of Fe_2O_3 taken initially, and its condition after compaction (during the preparation of green compact) may vary I_{Fe} and I_O values from the sample to sample.

From the values of P and R one can see that I_B is least as compared to I_A and I_C . Since I_A , I_B , I_C signify the reduction of different oxide phases, the above calculation

demonstrates clearly that reaction rate is least in Fe_3O_4 phase. It may, therefore, be proposed that the overall reduction reaction is controlled by the reaction taking place at the hematite-magnetite phase boundary, a proposition which is similar as given by Bradshaw and Matyas⁽¹⁵⁾.

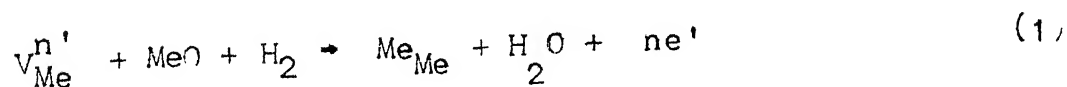
3.3 FORMATION AND GROWTH OF IRON, NICKEL AND COPPER NUCLEI DURING GASEOUS REDUCTION OF THEIR OXIDES

3.3.1 Introduction

The oxides of iron, copper and nickel are non-stoichiometric. Wustite (Fe_xO) has sodium chloride type face centered cubic structure with metal ion vacancies. Cuprous oxide (Cu_2O) has simple cubic structure with metal ion vacancies. Nickel oxide (NiO) has sodium chloride type structure. It is a p-type semiconductor and has excess oxygen over the stoichiometric amount⁽²¹⁾. In contrast to their oxides γ -iron, copper and nickel have all face centered cubic structures. The orientation relationships between Fe, Ni and their oxides FeO, NiO are as follows:

- (i) Wustite/Iron: $(100)_{\gamma\text{-Fe}} \parallel (100)_{\text{FeO}}; (010)_{\gamma\text{-Fe}} \parallel (011)_{\text{FeO}}$
- (ii) Nickel oxide/ nickel : $(111)_{\text{Ni}} \parallel (111)_{\text{NiO}}; (001)_{\text{Ni}} \parallel (001)_{\text{NiO}}$

No orientation relationships have been suggested between copper and copper oxide but they are expected to be similar to Fe and Ni. The habit plane for the metal nuclei to grow from the oxide face according to the reaction



should be (111) because of their closest packing; $V_{\text{Me}}^{n'}$ is the ionized metal vacancy, n is the charge of vacancy, e' is the

free electron and Me_{Me} is the Me atom in MeO in its normal lattice site.

Oxide requires certain amount of supersaturation with respect to the metal at the MeO-Me interface before nucleation can occur and this is achieved by diffusion of metal to the MeO-Me interface. The reduced metal vacancy concentration at the MeO/H₂ interface and the corresponding supersaturation with respect to metal provides the driving force for metal diffusion which is evident from equation (1).

According to Wagner⁽²⁹⁾, the diffusion paths in an oxide or sulphide subjected to reduction are rather involved. Initially one may assume that the area of the metal oxide-metal interface is much smaller than the area of the metal oxide surface in contact with hydrogen gas. Under these conditions, most of the diffusion resistance is concentrated in the contact areas between the oxide and metal. The expression for rate of transport of metal from outer surface of metal oxide to the contact areas adjacent to the growing nuclei given by Wagner⁽²⁹⁾ is,

$$\dot{n}_{\text{Me}} \approx \frac{4A C_{\text{Me}} D_{\text{Me}}}{r_{\text{f Me}}} \ln \left(\frac{a_{\text{Me}}^{\text{I}}}{a_{\text{Me}}^{\text{II}}} \right) \quad (2)$$

where,

A = total area of contact between the oxide and metal

- r = average radius of the individual contact area
 C_{Me} = average concentration of Me in MeO
 D_{Me} = self diffusion coefficient of Me in MeO
 f_{Me} = correlation factor for Me in MeO which may be taken to be unity for our study
 a_{Me}^I = activity of Me in MeO at the MeO/H₂ interface
 a_{Me}^{II} = activity of Me in MeO adjacent to the Me particles.

Since a_{Me}^{II} is unity, a_{Me}^I must be greater than one (supersaturation) to obtain positive growth rates in accordance with equation (2). As the nuclei grows its shape may change depending upon the interplay of metal ion diffusion (D_{Me}) and the rate of the reaction (1) i.e., oxygen removal from the surface of the oxide by the reducing gas. In the present work, both the shape and growth rates of Fe, Ni and Cu were studied during the initial stages of reduction.

3.3.2 Results and Discussion

A characteristic feature of the morphology of the Fe, Ni and Cu nuclei growing on their respective FeO, NiO and Cu₂O oxide surfaces, as observed in the present work, was that they were all generally of the shape of tetrahedral based pyramid (except during very initial stages of the formation). In some cases the faces of the pyramid were equilateral triangles (i.e., angles were 60°) and in some cases right angled triangles (the angle at the pyramid apex was 90°). The sizes of the nuclei were however different depending upon type of

metal (Fe, Ni or Cu), time and temperature of reduction. Both the shape and size of nuclei can be explained in terms of orientation relationships, habit planes, metal ion diffusion and rate of removal of oxygen from the oxide surface.

(a) Shape of the Nuclei:

The shape of the nucleus in the very early stages of reduction is expected to be a thin disc⁽³⁰⁾ so as to minimise the strain energy [Fig. 3.3 (a)]. Subsequently, metal nuclei can grow either laterally covering the oxide surface, or in a direction perpendicular to the surface of the oxide. The lateral growth of nuclei can take place under pure metal transport control⁽¹⁰⁾. In this case the capacity of metal ion production at the oxide surface is very high as compared to its capacity of transport from the surface inwards, resulting in metal ion build-up at the surface. Diffusion of metal ions being slow in all directions there is hardly any supply of metal ion from the bulk to feed to nucleus. So the metal ions migrate along the surface of the oxide and accumulate at the periphery of the nucleus resulting in lateral growth as shown in Figure 3.3(b). Vertical growth of nuclei can take place under pure oxygen removal control of the reaction⁽¹⁰⁾. In this case the rate of metal ion transport is much higher than the rate of metal ion production at the surface. So there is considerable feeding of metal ions from the bulk to the nucleus resulting in growth of the nucleus as a whisker as shown in Figure 3.3(c). A combination of lateral and vertical growth

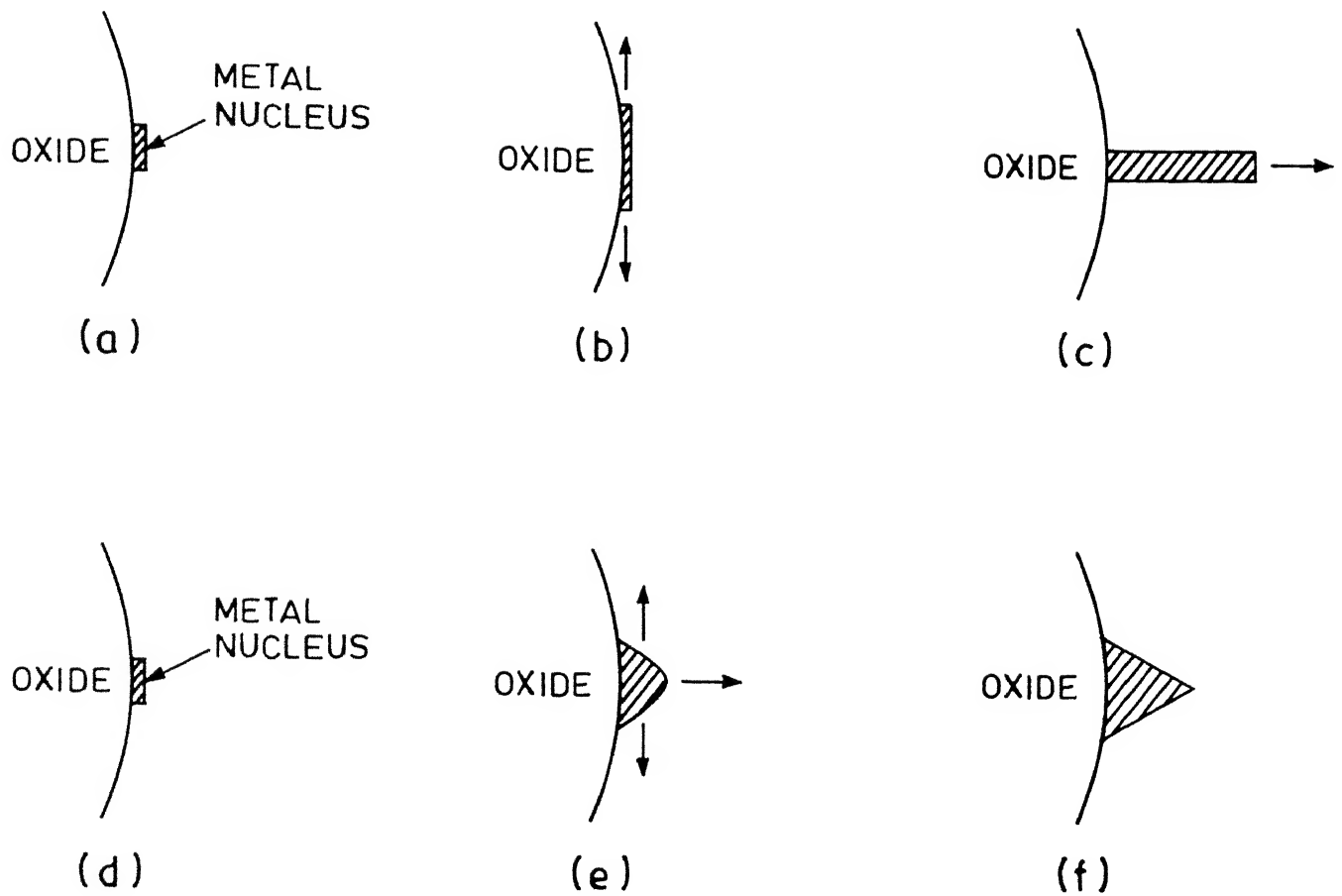


Fig. 3.3. Shape of the growing metal nuclei during reduction

- (a) Initial shape
- (b) Under pure x transport control
- (c) Under pure oxygen removal control
- (d) Initial shape
- (e) & (f) Under mixed control.

as depicted in Figure 3.3(d), (e), (f) can ultimately result in a pyramid as observed in the present work; Figs. 3.5 to 3.7 show the growth of iron nuclei on wustite during hydrogen reduction of hematite compacts at 1423K.

In Figure 3.5, the nuclei are in the form of a disc with slight bulge at the apex; in Figure 3.6 the nuclei have grown laterally as well as vertically; in Figure 3.7 the growing nuclei have taken the pyramidal shape. Dube and Deo⁽¹⁹⁾ observed similar shape of the grown nuclei during hydrogen reduction of magnetite compacts at 1423K [see Figure 4, Ref. 19].

Figure 3.8 shows some pyramidal shaped nickel nuclei during hydrogen reduction of nickel oxide at 1423K. Figure 3.9 shows a similar feature for the copper nucleating on Cu_2O during hydrogen reduction at 873K. Veistaro et.al.⁽²²⁾ also reported similar shape of copper nuclei during Cu_2O reduction study by hot stage scanning electron microscopy at 1068K in 50% H_2 - 50% N_2 atmosphere. In fact, he obtained very sharp featured pyramidal copper nuclei [see Figure 13, Ref. 22].

Figure 3.4 schematically shows the tetrahedral base pyramid ABCDE similar to the observed pyramid shown in Figures 4 and 5 of Ref. 3. Here two $\{111\}$ planes viz., ABD and DBC are the base of the pyramid (habit planes). Two $\{100\}$ planes viz., EBC, DEC and two $\{110\}$ planes AED, ABE intersect to form the four faces of the pyramid. The apex angles of $\{100\}$ and $\{110\}$ planes are 90° and 60° respectively. Both of these apex angles were observed

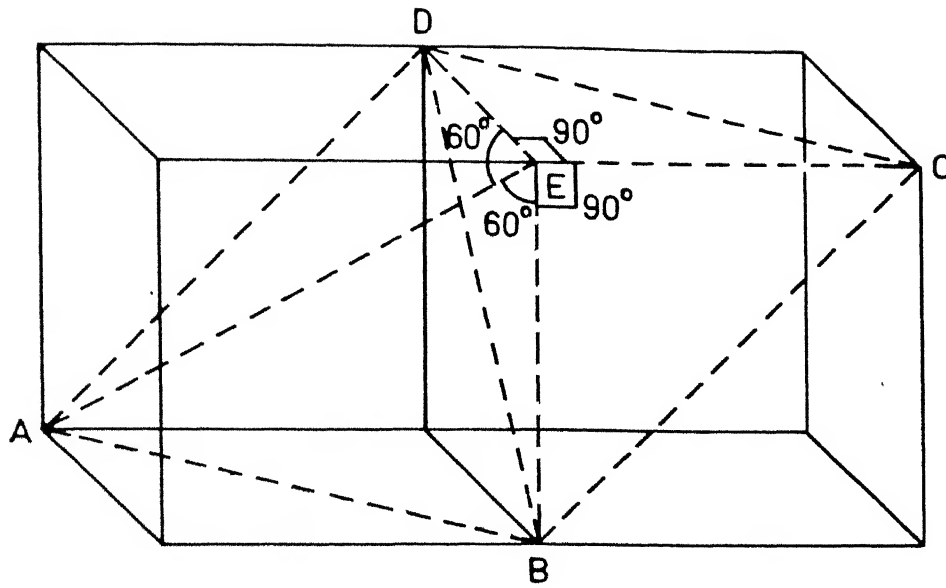


Fig. 3.4. Schematic diagram showing tetrahedral based pyramid in fcc unit cells

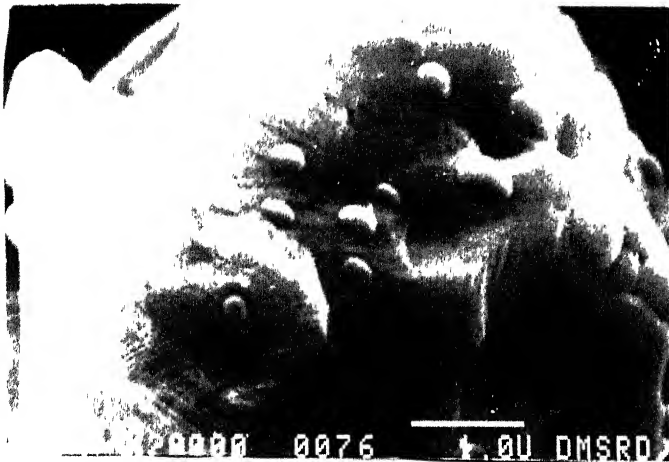


Fig. 3.5 : SEM of the interfacial region of the partially reduced hematite (Reduction temp-1423K, Reductant - H_2) showing very first stage of nucleation.



Fig.3.6 : SEM of subsequent growth of the iron nuclei in Fig.3.5 in the vertical direction leading to a bulge.



Fig. 3.7 : SEM of iron nuclei grown into a tetrahedral based byramid.



Fig. 3.8 : SEM of the interfacial region of partially reduced nickel oxide (Reduction temp., -1423K, Reductant -H_2) showing tetrahedral based pyramid shaped nickel nuclei.

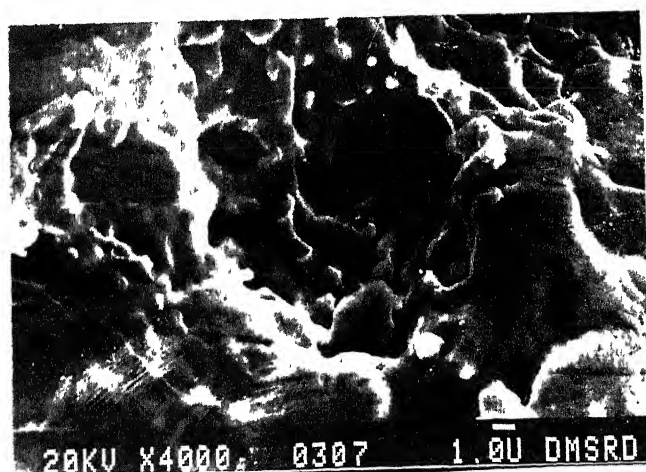


Fig. 3.9 : SEM of the interfacial region of partially reduced cuprous oxide (Reduction tem. -1423K, Reductant -H_2) showing tetrahedral based pyramid shaped copper nuclei.

(visually) in the present work confirming that habit plane is of $\{111\}$ type and the growth planes are of $\{100\}$ or $\{011\}$ type for Fe, Ni and Cu. Cech⁽⁷⁾ also observed that in the case of nickel the growing crystallites are either parallel to (100) or (110) of NiO.

(b) Growth Rate of the Nuclei:

The growth mechanism of the hemispherical shape of metal nuclei as suggested by Ramanarayanan et.al.⁽³¹⁾ is shown in the Figure 3.10. In the present work the nuclei shape was pyramidal and therefore a hemisphere of equal volume has been considered as a first approximation.

For hemispherical particles,

$$\dot{n}_{Me} = \frac{dn_{Me}}{dt} = \frac{2\pi r^2 K}{V_{Me}} \cdot \frac{dr}{dt} \quad (3)$$

where V_{Me} is the molar volume of Me; K is the number of 'Me' particles per unit area of the surface; r is the particle radius and t is the time of reduction.

Thus equation (3) can be rewritten as

$$r dr \approx 2 C_{Me} D_{Me} V_{Me} \ln(a_{Me}^I) dt \quad (4)$$

On integrating equation (4),

$$r = [4 C_{Me} D_{Me} V_{Me} \ln(a_{Me}^I) t]^{1/2} \quad (5)$$

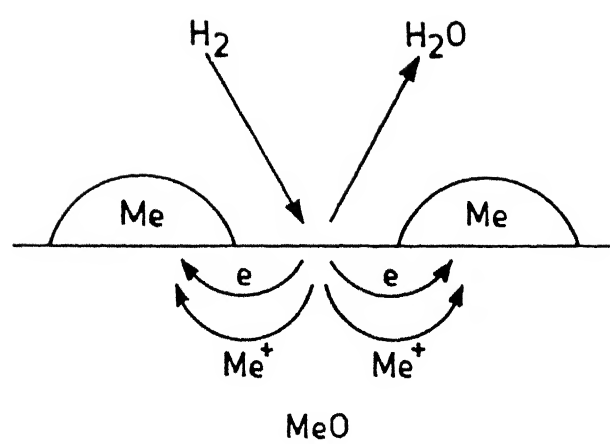


Fig. 3.10. Mechanism of reduction of MeO to Me.

From this relationship one can calculate nuclei sizes at different times. For nickel oxide reduced by hydrogen at 1423K, the parameters are, $D_{Ni} = 1.784 \times 10^{-10} \text{ cm}^2 \text{ sec}^{-1}$; $C_{Ni} = 0.5$; $V_{Ni} = 6.588 \text{ cm}^3 \text{ mole}^{-1}$; $t = 300 \text{ sec}$; $a_{Ni}^I = 1.0005$ and substituting these in equation (5),

$$r_{Ni}^{1423} = 0.138 \mu\text{m}.$$

Nuclei of nickel of almost the same size were observed in the present study as shown in Figure 3.8.

In the case of reduction of Cu_2O by hydrogen at 873K, the parameters are, $D_{Cu} = 1.099 \times 10^{-10} \text{ cm}^2 \text{ sec}^{-1}$; $C_{Cu} = 0.67$; $V_{Cu} = 7.1128 \text{ cm}^3 \text{ mole}^{-1}$; $t = 360 \text{ sec}$. and $a_{Cu}^I = 1.0005$ and substituting these in equation (5), one obtains,

$$r_{Cu}^{873} = 0.195 \mu\text{m}.$$

The calculated value of the size of copper nuclei is slightly lower than the experimentally observed (Fig.3.9) value. It may be attributed to the fact that Cu_2O was prepared by adding stoichiometrically excess copper to CuO . During hydrogen reduction this excess copper perhaps increases the nucleation and growth rate by helping metal ion supersaturation in the oxide phase to be achieved more rapidly.

In the case of hydrogen reduction of FeO at 1423K, the parameters are $D_{Fe} = 3.19 \times 10^{-7} \text{ cm}^2 \text{ sec}^{-1}$; $C_{Fe} = 0.5$; $V_{Fe} = 7.0948 \text{ cm}^3 \text{ mole}^{-1}$; $t = 180 \text{ sec}$; $a_{Fe}^I = 1.0005$.

One obtains from equation (5)

$$r_{Fe}^{1423} = 6.362 \text{ } \mu\text{m}.$$

This theoretically computed value of the size of the iron nuclei is much greater than the experimentally observed value of $0.6 \text{ } \mu\text{m}$ (as shown in Figure 3.7). During hematite reduction intermediate oxides Fe_3O_4 and FeO are formed. Hematite is at the centre and iron forms at the surface. For solid state reduction of hematite and magnetite, iron has to diffuse inwards from surface to the hematite-magnetite and the magnetite wustite interfaces respectively. Thus iron concentration at the surface is doubly decreased causing less iron feeding to the iron nuclei. Probably this is manifested in a smaller size iron nuclei than the theoretically predicted value from equation (5).

(c) Reduction of Dicalcium Ferrite Compacts:

Dicalcium ferrite ($2 \text{ CaO} \cdot \text{Fe}_2\text{O}_3$) has an orthorhombic structure and it is known to get reduced directly to iron without the formation of intermediate oxide phases viz., Fe_3O_4 and FeO. The shape of the nuclei of iron formed on the parent

dicalcium ferrite particles also appears to be a tetrahedral based pyramid (Figure 3.11). By analogy with FeO , NiO and Cu_2O one can, therefore extrapolate that during the reduction of dicalcium ferrite compacts the habit plane is $\{111\}$ type while the growth planes are of $\{100\}$ and $\{011\}$ type. This however needs to be confirmed by further experimentation.

Since no information is available in literature on the diffusion coefficient of iron in dicalcium ferrite the size of iron nuclei could not be calculated.

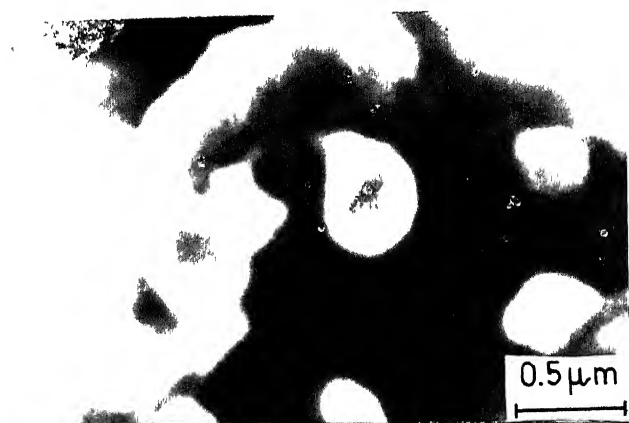


Fig. 3.11 : SEM of the interfacial region of partially reduced di-calcium ferrite (Reduction temp. -1423K, Reductant - H_2) showing tetrahedral based pyramid shaped iron nuclei.

3.4 MORPHOLOGY OF THE REDUCTION PROCESS

3.4.1 Reduction of Iron Oxide Compacts

When magnetite and hematite compacts were reduced with hydrogen at 1423K, two distinguishable zones were observed, viz., reduced zone and unreduced zone with a diffused interface between them. However, a few particles in the unreduced zone were been either fully or partially reduced. Figure 3.12 shows the starting hematite compact particles had no porosity or cracks. Figure 1 of reference (19) shows similar feature for magnetite compact.

Figure 3.13 shows the optical micrograph of the polished specimen of partially reduced hematite in the unreduced zone showing extensive fragmentation of parent hematite particle. Figure 3.14 shows the scanning electron micrograph of a similar particle showing extensive cracking and fragmentation of the parent particle.

Figure 3.15 shows a typical optical micrograph of the parent magnetite particles in a partially reduced magnetite compact in the unreduced zone.

It can be seen that in the case of magnetite compacts, there is relatively lesser degree of cracking and fragmentation of the parent particle as compared with that of hematite compacts. [Figures 3.13 and 3.15] .



Fig. 3.12 : SEM of hematite concentrate powder, showing no porosity.

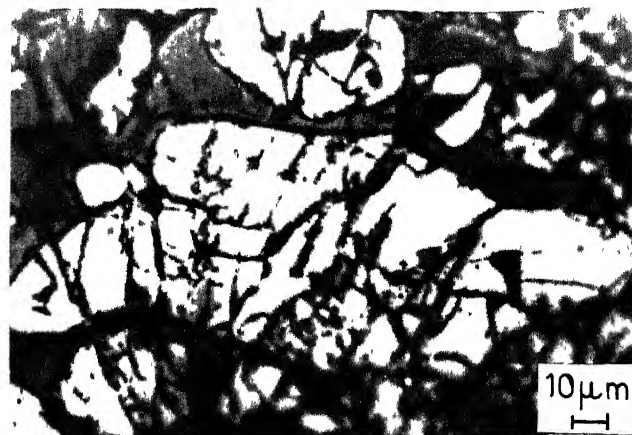


Fig. 3.13 : Optical micrograph of unreduced zone of partially reduced hematite (Reduction temp. -1423K, Reductant $-H_2$) showing fragmentation of oxide particles.



Fig. 3.14 : SEM of partially reduced hematite (Reduction temp. -1423K, Reductant $-H_2$) fragmentation of particles in the interfacial region.

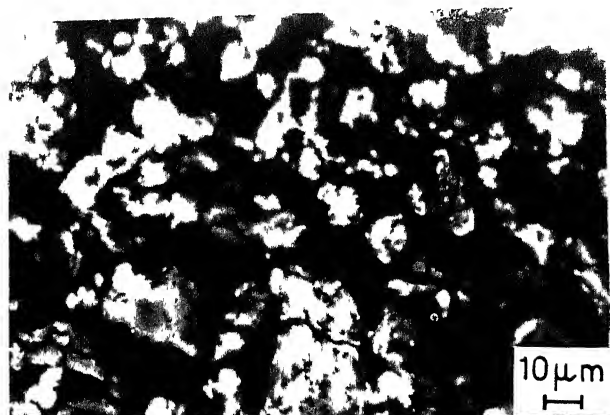


Fig. 3.15 : Optical micrograph of partially reduced magnetite at the unreduced zone (Reduction temp. -1423K, Reductant $-H_2$) showing less cracking tendency of the oxide particles.

Hematite has a rhombohedrally centred hexagonal lattice while the magnetite is an inverse spinel type structure, which possess the cubic symmetry. During reduction of magnetite, its crystallographic orientation relationship with its lower oxide are such that magnetite to wustite is carried out in a manner that the crystallographic axes of the three cubic systems remain mainly parallel to each other. During hematite reduction initial hexagonal to cubic lattice transformation incurs distortion resulting in severe cracks.

(28)

According to Bitsianes and Joseph during hematite reduction there is a relationship between planes of hematite and magnetite like $(0001)_H \parallel (111)_M$. So, during transformation there is a drastic shift in the position of main crystallographic axis. The magnetite grows as crystallites on the hematite surface by considerable particle fragmentation. This feature is preserved during the subsequent reduction.

As reported earlier, Figure 3.16 shows the optical micrograph of the interface between reduced zone and unreduced zone of partially reduced magnetite compact. [Reduction temperature -1423 K, Reductant - H_2].

Due to fragmentation and cracking the reducing gases are accessible not only to the surface but also inside the magnetite particles from various directions, the extent of which depends on ^{the} degree of cracking and fragmentation. For example, the reduction of a magnetite particle would be more in the vicinity of the hole formed on the surface of the particle shown by point A on the Figure 3.16.

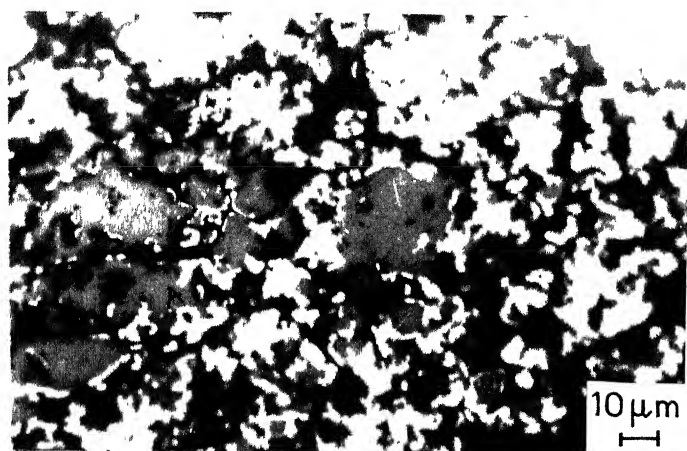


Fig.3.16 : Optical micrograph of partially reduced magnetite (Reduction temp. -1423K , Reductant $-\text{H}_2$) showing interface between reduced zone and unreduced zone.

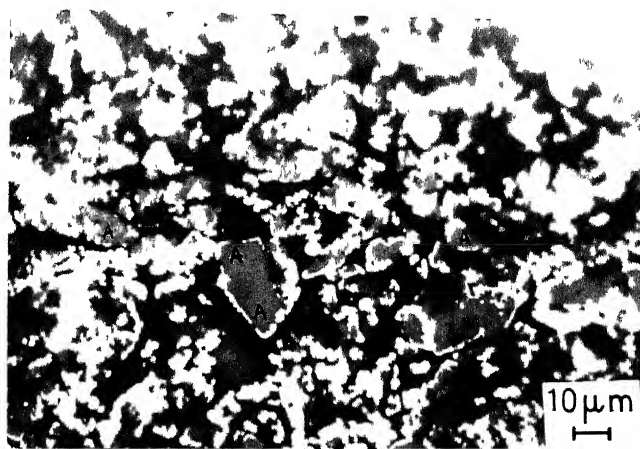


Fig.3.17 : Optical micrograph of partially reduced magnetite (Reduction temp. -1423K , Reductant $-\text{H}_2$) showing some discontinuities during very early stage of iron formation on wustite.

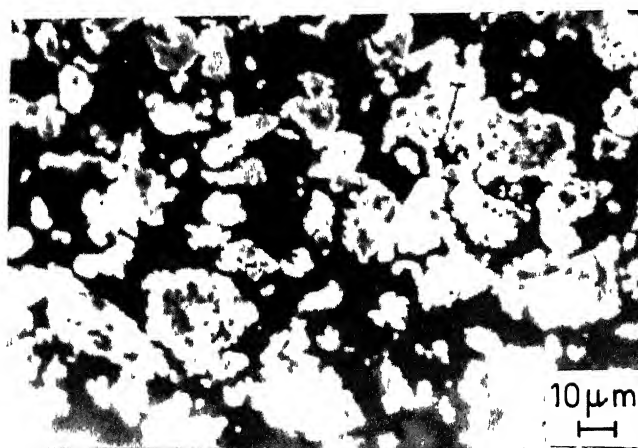


Fig. 3.18 : Optical micrograph of partially reduced magnetite (Reduction temp. -1273K , Reductant $-\text{H}_2$) showing topochemical reduction of oxide particles.

Another interesting observation which can be made is that in the very initial stages of reduction of particle the grown islands of iron do not completely cover the wustite particle. There are discontinuities, either wide or narrow. The reason for this is ^{that the} formation of iron on wustite takes place where the supersaturation of iron in wustite reaches the critical value for nucleation. It seems that the supersaturation of iron has not reached uniformly over the surface of parent oxide. This would also be caused due to the fact that the bulk diffusion of iron predominates at higher temperatures (1423K) and it is expected that the nuclei formed will grow in vertical direction (i.e. perpendicular to the surface) and the supersaturation in the regions between the originally formed nuclei will not be built-up which is needed for additional nuclei to form. This behaviour results into small discontinuities in the iron islands formed on wustite surface, as marked by point A in Fig. 3.17.

During reduction of magnetite compacts at 1273K by hydrogen it was observed that there was no interface between the reduced zone and unreduced zone and instead the entire cross section of the compact formed the reaction interface. In other words each individual particles of magnetite started getting reduced simultaneously, in a topochemical manner as shown in Figure 3.18.

Reduction morphology depends on the intrinsic chemical reactivity of the oxide particles. The intrinsic chemical reactivity in turn depends on reduction temperature, particle size of parent oxide, initial porosity etc.

During the course of reduction of magnetite compacts, the reducing gases have to diffuse inside the compact through interparticle porosity. If the intrinsic chemical reactivity of the magnetite particles are high, then all the reducing gases would be consumed by the oxide particles and the reduction would slowly propagate from the surface to the core of the compact. This behaviour would result in the reduction of compact as a whole in a topochemical manner, and a reaction interface would result between the reduced zone and the unreduced zone. Such a behaviour seems to occur during the reduction of magnetite at 1423K.

On the other hand, if the intrinsic chemical reactivity of the magnetite particles is low, then the layer of magnetite particle exposed to the reducing gases will reduce slowly, and therefore the reducing gases will move ahead of the layer. This phenomenon will continue and very soon the reducing gases would be accessible to all the magnetite particles covering the entire cross-section. This behaviour would not result in the reduction of compacts as a whole in a topochemical manner. However, each particles have reduce in a topochemical manner, as shown in Figure 3.18. Such a behaviour has been observed

at the reduction temperature of 1273K.

At the lower temperature (1273K) the vertical growth of iron nuclei on wustite surface would be slow and the supersaturation in iron due to surface reduction of wustite in the neighbouring regions build-up leading to further iron nuclei formation. In such cases there would be a large number of small nuclei formed on the surface of wustite. Such a behaviour has been reported earlier by Dube and Deo⁽¹⁹⁾. Eventually such behaviour would result in the formation of a dense iron layer covering the entire surface of wustite.

Figure 3.19 shows the optical micrograph of the interface between reduced zone and unreduced zone of partially reduced hematite compact (Reduction temperature -1423K, reductant - H_2).

Reducing gas had access not only to the surface but also inside the parent oxide particles from different direction due to fragmentation and cracking. In the initial stages of reduction of a particle the grown islands of iron do not completely cover the wustite particle leaving some discontinuities as shown by point A on Figure 3.19.

The morphological features during hydrogen reduction of hematite compacts at 1423K are more or less similar to that during hydrogen reduction of magnetite compacts at 1423K and similar explanation can be given for this feature as for magnetite compact reduction.

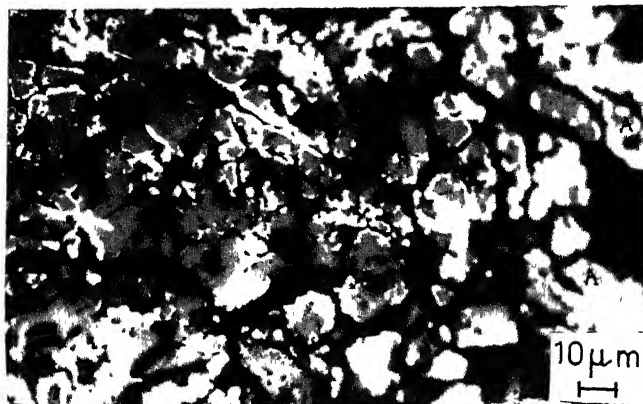


Fig. 3.19 : Optical Micrograph of the interface in partially reduced hematite (Reduction temp. -1423K, Reductant -H₂) showing reduced zone and unreduced zone.

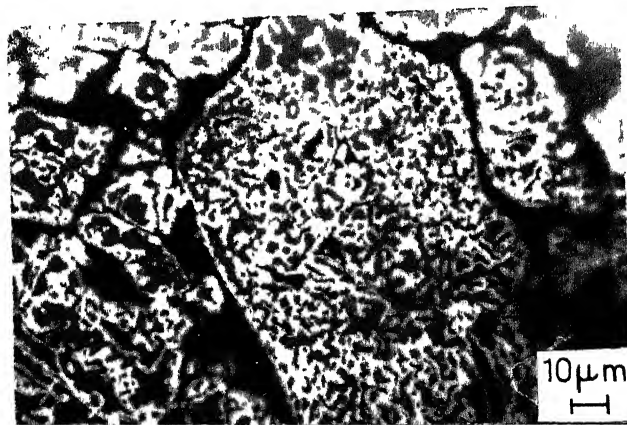


Fig. 3.20 : Optical Micrograph of partially reduced hematite (Reduction temp. -1098K, Reductant -H₂) showing topochemical reaction on individual particles.

Hematite was reduced in hydrogen at temperatures 1373K, 1273K, 1173K and 1123K, but in all the cases diffused reaction interface between reduced zone and unreduced zone was obtained. When reduction was performed at 1098K there was no interface but instead the reduction has started throughout the entire cross section of the compact as shown by Figure 3.20. As stated earlier during hematite reduction there is a considerable amount of fragmentation and cracking leading to particle size refinement which in turn results in higher intrinsic chemical reactivity than magnetite at the same temperature of reduction. So, during hydrogen reduction of hematite compact from 1123K onwards the intrinsic chemical reactivity of parent oxide particles reaches such a high value that reducing gas can advance only to a certain distance before it gets consumed by the reaction taking place at the interface of the reduced and the unreduced region.

Figure 3.20 shows severe cracking of hematite particles during hydrogen reduction of hematite compacts at 1098K. Reduced metals have started forming heterogeneously at these cracks. Here individual particles are reduced more or less topochemically throughout the cross section. However, at certain places this topochemical nature is disrupted due to the presence of cracks as higher reducing conditions prevail along these cracks. So on these particles reduction progresses ahead of the normally advancing reduction interfaces.

3.4.2 Reduction of Nickel Oxide Compacts

Figure 3.21 shows the optical micrograph of the interface between the reduced zone and the unreduced zone of the partially reduced nickel oxide compact reduced with hydrogen at 1423K.

This feature is similar to that observed during high temperature (1423K) reduction of hematite and magnetite compacts with hydrogen. As stated earlier for iron oxide reduction, here also the intrinsic chemical reactivity of the nickel oxide particles are high at this temperature (1423K) and, as a result, the reducing gases are consumed by the oxide particles. Eventually, this leads to a continuously moving reduction interface from surface to the core of the compact in a topochemical manner.

Figure 3.22 shows the optical micrograph of partially reduced nickel oxide compacts during hydrogen reduction at 823K. In this case no interface was observed between the reduced zone and ^{the}unreduced zone, but instead the entire cross section of compact formed the reaction interface. This behaviour can be correlated to low intrinsic chemical reactivity of the nickel oxide particle and similar explanations can be given for this behaviour as given during magnetite reduction at 1273K and hematite reduction at 1098K.

Figures 3.23 and 3.24 show partially reduced area and fully reduced area during hydrogen reduction of nickel oxide

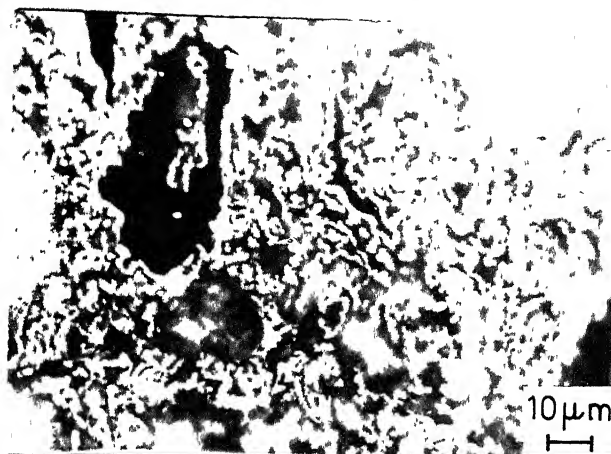


Fig. 3.21 : Optical micrograph of the interface of partially reduced nickel oxide (Reduction temp. -1423K, Reductant -H_2) showing reduced zone and unreduced zone.

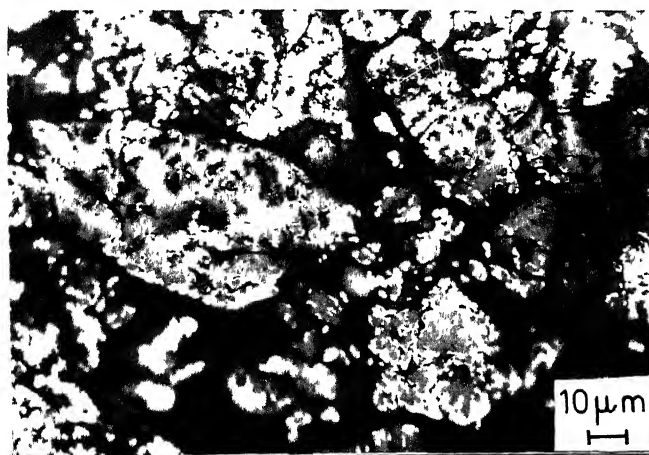


Fig. 3.22 : Optical micrograph of partially reduced nickel oxide (Reduction temp. - 823K, Reductant -H_2) showing topochemical reduction of oxide particles.

at 1423K. These figures show typical wavy fibres of nickel formed during nickel oxide reduction. One may correlate this feature to the formation of long stringers during the nickel oxide reduction process, though its confirmation requires more study in this field. This structure essentially becomes dense due to concurrent sintering taking place during reduction as shown in Figure 3.25.

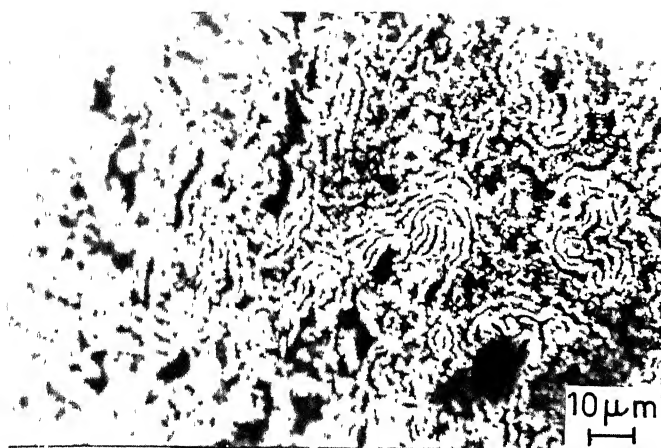


Fig. 3.23 : Optical micrograph of partially reduced nickel oxide in the interfacial zone (Reduction temp.-1423K, Reductant $-H_2$) showing long wavy stringers.

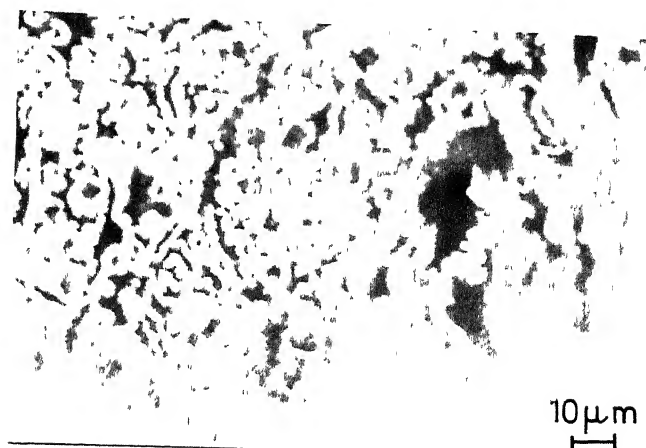


Fig.3.24 : Optical micrograph of partially reduced nickel oxide in the fully reduced zone (Reduction temp.-1423K, Reductant $-H_2$) showing wavy stringer structure of the nickel.

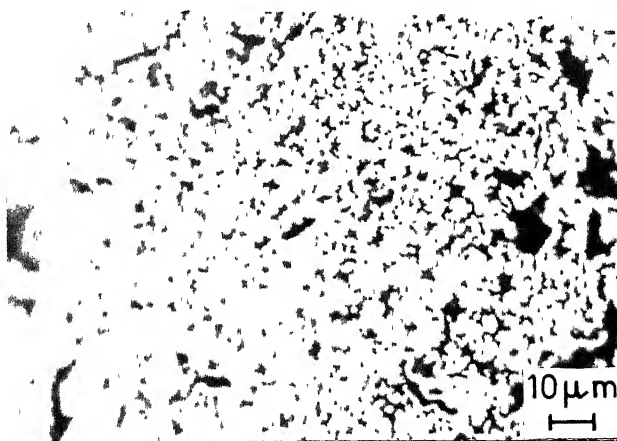


Fig. 3.25 : Optical micrograph of partially reduced nickel oxide (Reduction temp. -1423K, Reductant $-H_2$) showing dense nickel structure.

CHAPTER 4

CONCLUSIONS

- (1) Mathematically it is proved that the layer of magnetite formed on hematite has to be porous or fragmented for the topochemical reduction sequence hematite \rightarrow magnetite \rightarrow wustite.
- (2) At 823K the kinetics of formation of magnetite from hematite by solid state reduction by iron is proved to be very slow.
- (3) Since slitting and fragmentation are shown to occur in the reduction step magnetite \rightarrow wustite as well the increase in porosity (or volume fraction) per mole of iron is of the order of 2.5.
- (4) Equivalent rates of iron and oxygen transfer through different oxide phase boundaries during hydrogen reduction of hematite are calculated at temperatures 1023 and 1123K. The rates show an increasing tendency with temperature.
- (5) It is proposed that hydrogen reduction of hematite at 1023 and 1123K are controlled by the step of the reaction occurring at hematite-magnetite interface.
- (6) The nuclei of the FCC metals (Fe(γ), Ni, Cu) during hydrogen reduction of FeO, NiO and Cu₂O respectively grow initially as a disc and gradually change over to tetrahedral based pyramids. This particular type of metal nuclei growth pattern is correlated to the

mixed control mechanism of metal ion transport within the oxide particle and rate of oxygen removal from the surface of the oxide particle by hydrogen.

- (7) In the tetrahedral based pyramid the habit plane is shown to be {111} type and growth planes are of {100} and {011} type.
- (8) A model for the growth rate is used to calculate Fe, Ni and Cu nuclei sizes at different times. For Ni and Cu nucleation this model closely matches with the observed sizes of nuclei while for iron nucleation a low experimentally observed value is explained in terms of larger iron ion migration (compared to Cu_2O and NiO) from the surface (FeO) to the core (Fe_2O_3) via intermediate Fe O_4 .
- (9) For hydrogen reduction of dicalcium ferrite at 1373K, the shape of the iron nuclei is also a tetrahedral based pyramid. So, by analogy with hematite reduction {111} type planes is proposed to be the habit plane with {100} and {011} type planes as growing planes.
- (10) Considerable amount of cracking and fragmentation of particles take place during reduction of hematite compact as compared to magnetite particles during reduction. This is attributed to drastic shift in the position of the main crystallographic axis resulting in lattice distortion during hematite to magnetite transformation.

- (11) During very initial stages of both hematite and magnetite^{reduction} at high temperature (1423K) there are some discontinuities in the iron formed on the parent oxide particle surface. This feature is explained in terms of vertical growth of iron at that temperature and lack of supersaturation formation of iron nuclei at those discontinuities.
- (12) At high temperature (1423K) the compact as a whole is reacting topochemically for both hematite and magnetite compacts. At low temperature (1273K for magnetic and 1098K for hematite) the reduction is taking place simultaneously throughout the entire cross section, however individual particles do react topochemically. This morphological feature is explained in terms of^{the} variation in intrinsic chemical reactivity of the oxides at the temperatures.
- (13) Similar observations as in (12) are made during reduction of nickel oxide compacts at 1423K and 823K by hydrogen.
- (14) The morphology of nickel formed on nickel oxide at 1423K is correlated to formation of long stringers during the reduction of nickel oxide. However, these stringers sinter together at various contact points, leading to a relatively dense structure.

CHAPTER 5

RECOMMENDATION FOR FUTURE WORK

1. More detailed experimentation is required for copper oxide and dicalcium ferrite reduction.
2. Similar studies can be made for other metals whose powders are produced by oxide reduction, like W, Mo, etc.
3. Microstructural features can be correlated with kinetic data obtained during reduction by performing the reduction test in a thermogravimetric set-up. Activation energy data can be compared with the morphological evidences to confirm the controlling mechanism for the reduction reaction.
4. Pore morphology of the powder obtained after grinding the reduced metal cake should be studied in detail , which governs the subsequent compaction behaviour.
5. Hot stage scanning electron microscopy can be used to observe the morphological changes occurring during the reduction in-situ.

REFERENCES

- (1) Smithells, Metals Reference Book, 2, 4th ed., New York, Plenum Press.
- (2) Bogdandy, Von, L.; Engell, H.J. : The Reduction of Iron Ores, Springer Verlag, Berlin, 1971, pp. 36-39.
- (3) Hansen, M. : The Constitution of Binary Alloys, 2nd ed., New York/Toronto/London, 1958.
- (4) Roller, P.W. : Trans. ISIJ, 26, (1986), pp.834-5.
- (5) *ibid* ref. 2, pp. 30-1.
- (6) Roth, W.L. : Acta Crystallogr., 13 (1960), pp.140-9.
- (7) Gorton, A.T.; Bitsianes, G. ; Joseph, T.L. : Trans. Met. Soc. AIME, 233 (1965), pp. 1519-25.
- (8) Volmer, M. ; Weber, A. : Z. Phys. Chem., 119, (1926), pp. 277-301.
- (9) Wagner, C. : Trans. Met. Soc. AME, 194, (1952), pp. 214-6.
- (10) Nicolle, R.; Rist, A. : Met. Trans. B, 10B, Sept (1979), pp. 429-38.
- (11) Edström, O.J. ; Bitsianes, G. : Journal of Metals, 7, (1955), pp. 760-5.
- (12) Warner, N.A. : Trans. Met. Soc. AIME, 230, (1964), pp. 163-76.
- (13) Turkdogan, E.T.; Vinters, J.V. : Met. Trans. , , 3, June (1972), pp. 1561-74.
- (14) Li, K.; Trushenski, S.P.; Philbrook, W.O. : Met. Trans., 5, (1974), pp. 1149-58.
- (15) Bradshaw, A.V.; Matyas, A.G. : Met. Trans.B, 7B, March (1976), pp. 81-7.
- (16) St. John, D.H.; Hayes, P.C. : Met. Trans. B, 13B, March (1982), pp. 117-24.
- (17) Moukassi, M., Dupre, B.; Gleitzer, C. : Met. Trans. B, 14B, March (1983), pp. 125-32.

- (18) St. John, D.F.; Mathew, S.P.; Hayes, P.C. : Met. Trans. B, 15B, Dec. (1984), pp. 701-8.
- (19) Dube, R.K.; Deo. B. : Steel Research, 58, No. 9, (1987), pp. 395-8.
- (20) Cech, P.E. : Trans. Met. Soc. AIME, 215, Oct. (1959), pp. 769-81.
- (21) Little, J.A.; Evans, J.W.; Westmacott, K.H. : Met. Trans. B, 11B, Sept. (1980), pp. 514-24.
- (22) Veistaro, M.; Harkki, J.; Tikkanen, M.H. : Scand. J. Metallurgy, 8 (1979), pp. 6-9.
- (23) Mankhand, T.R.; Rao, V.V.P.K. ; Prasad, P.M. : Metallography, 14, (1981), pp. 335-45.
- (24) Bhargava, S.; Dube, R.K. : Mat. Sc. & Tech., 1, Sept. (1985), pp. 743-7.
- (25) Laboratory Type Lectrodryer, Instruction Manual, Lectrodryer Division, Ajax Magnethermic Corporation, Richmond, Kentucky.
- (26) ibid Ref. 2, pp. 89-91.
- (27) Schwenk, W.; Rahmel, A. : Oxidation of Metals, 25, Nos. 5/6, (1986), pp. 293-303.
- (28) Bitsianes, G.; Joseph, T.L. : Journal of Metals, May (1955), pp. 639-45.
- (29) Wagner, C. : Steel Making, The Chipman Conference, Elliot, J.F. ed., M.I.T. Press, 1965, p. 19.
- (30) Habarro, F.N. : Proc. Phys. Soc., 52 (1940), pp. 90-3.
- (31) Ramanarayanan, T.A.; Alonzo, J. : Oxidation of Metals, 24 (1985), Nos. 5/6, pp. 17-27.